Dynamics of the Indian monsoon and ENSO relationships in the SINTEX global coupled model

Pascal Terray, Éric Guilyardi, Albert S. Fischer, Pascale Delécluse

To cite this version:

Pascal Terray, Éric Guilyardi, Albert S. Fischer, Pascale Delécluse. Dynamics of the Indian monsoon and ENSO relationships in the SINTEX global coupled model. Climate Dynamics, 2005, 24 (2-3), pp.145-168. 10.1007/s00382-004-0479-9 . hal-00124974

HAL Id: hal-00124974
https://hal.science/hal-00124974

Submitted on 27 Jun 2016

Dynamics of Indian Monsoon and ENSO relationships in the SINTEX Global Coupled Model

By
P. Terray (1,2), E. Guilyardi (3,4), A.S. Fischer (1) and P. Delecluse (1,3)

Submitted to *Climate Dynamics,* April 2003
Revised , April 2004

(1) LODYC, Paris, France
(2) Université Paris 7, Paris, France
(3) LSCE, Gif-sur-Yvette, France
(4) CGAM, Reading, UK

Abstract

This paper uses recent gridded climatological data and a coupled General Circulation Model (GCM) simulation in order to assess the relationships between the interannual variability of the Indian Summer Monsoon (ISM) and the El Niño-Southern Oscillation (ENSO). The focus is on the dynamics of the ISM-ENSO relationships and the ability of a state-of-the-art coupled GCM to reproduce the complex lead-lag relationships between the ISM and ENSO.

The coupled GCM is successful in reproducing the ISM circulation and rainfall climatology in the Indian areas even though the entire ISM circulation is weaker relative to that observed. In both observations and in the simulation, ISM rainfall anomalies are significantly associated with fluctuations of the Hadley circulation and 200 hPa zonal wind anomalies over the Indian Ocean. A quasi-biennial time-scale is found to structure ISM dynamical and rainfall indices in both cases. Moreover, ISM indices have a similar interannual variability in the simulation and observations.

The coupled model is less successful in simulating the annual cycle in the tropical Pacific. A major model bias is the eastward displacement of the western North Pacific Inter Tropical Convergence Zone (ITCZ), near the dateline, during northern summer. This introduces a strong semi-annual component in Pacific Walker circulation indices and central equatorial Pacific sea surface temperatures. Another weakness of the coupled model is a less-than-adequate simulation of the Southern Oscillation due to an erroneous eastward extension of the Southern Pacific Convergence Zone (SPCZ) year-round. Despite these problems, the coupled model captures some aspects of the interannual variability in the tropical Pacific. ENSO events are phase-locked with the annual cycle as observed, but are of reduced amplitude relative to the observations. Wavelet analysis of the model Niño34 time series shows enhanced power in the 2-4 year band, as compared to the 2-8 year range for observations during the 1950-2000 period.

The ISM circulation is weakened during ENSO years in both the simulation and the observations. However, the model fails to reproduce the lead-lag relationship between the ISM and Niño34 SSTs. Furthermore, lag correlations show that the delayed response of the wind stress over the central Pacific to ISM variability is insignificant in the simulation. These features are mainly due to the unrealistic interannual variability simulated by the model in the western North Pacific. The amplitude and even the sign of the simulated surface and upper-level wind anomalies in these areas are not consistent with observed patterns during weak/strong ISM years. The ISM and western north Pacific ITCZ fluctuate independently in the observations, while they are negatively and significantly correlated in the simulation. This isolates the Pacific Walker circulation from the ISM forcing. These systematic errors may also contribute to the reduced amplitude of ENSO variability in the coupled simulation. Most of the unrealistic features in simulating the Indo-Pacific interannual variability may be traced back to systematic errors in the base state of the coupled model.

1. Introduction

The relationships between the Indian Summer Monsoon (ISM) and the El-Niño Southern Oscillation (ENSO) have been widely documented for over 100 years. Indeed, the Southern Oscillation (SO) itself was first described by Walker (1923) in his search for ISM rainfall predictors. Since this pioneering work, the relationships between the ISM and ENSO have been investigated in many observational and modeling studies, but are still a controversial matter. Correlations between ISM rainfall and various ENSO indices suggest that anomalous monsoons are followed by significant ENSO-like fluctuations which provide very favorable conditions for triggering a cold or warm event in the Pacific the next winter (Elliott and Angell, 1987, Yasunari, 1990; Wang et al., 2001). This result has been confirmed by the modeling studies of Kirtman and Shukla (2000) and Kim and Lau (2001). On the other hand, some studies stress the passive role of the ISM in tropical variability, arguing that the broad scale dynamical monsoon is very sensitive to the phase of ENSO in the preceding spring (Rasmusson and Carpenter, 1983; Lau and Nath, 2000; Goswami and Jayavelu, 2001). Modulations in the intensity of the Inter-Tropical Convergence Zone (ITCZ) over the western Pacific in response to Sea Surface Temperature (SST) anomalies in the Pacific and Indian warm pool areas are thought to be important in this process (Ju and Slingo, 1995; Soman and Slingo, 1997; Kawamura, 1998). Despite these discrepancies, there is now abundant evidence that strong atmosphere-ocean-continental couplings are involved in ENSO-ISM relationships (Meehl, 1997; Meehl and Arblaster, 2002a,b). Thus, coupled General Circulation Models (GCMs) are possible tools to study ENSO-ISM interactions. Nevertheless the representation of interannual teleconnections remains a difficult challenge and may be biased by the ability of these coupled GCMs to realistically resolve the annual cycle in the Indo-Pacific region, since the annual cycle plays a dominant role in ISM-ENSO relationships (Webster et al., 1998, Ogasawara et al., 1999; Meehl and Arblaster, 2002a,b).

From the modeling perspective, the correct simulation by atmospheric GCMs of both seasonal and interannual fluctuations in ISM rainfall forced by observed SSTs is already a challenge (Sperber and Palmer, 1996; Gadgil and Sajani, 1998; Kang et al., 2002; Cherchi and Navarra, 2002). In many model experiments, the rain belt remains over the equatorial Indian Ocean in all seasons (Gadgil and Sajani, 1998). Others simulate excessive rainfall in the Indian region (Kang et al., 2002). It has been discovered that model ISM rainfall is sensitive to the physical parametrizations as well as numerics, resolution and the manner in which the orography is resolved in atmospheric GCMs (Fennessy et al., 1994; Slingo et al., 1994; Lal et al., 1997; Kang et al., 2002). There is considerable evidence that the simulation skill for monsoon rainfall interannual variability depends on the simulation skill of the annual cycle in the whole Indo-Pacific sector (Gadgil and Sajani, 1998; Kang et al., 2002). The interannual variability of ISM rainfall and circulation in coupled GCMs has also been investigated by many groups (Meehl and Arblaster, 1998; Kitoh et al. 1999; Meehl and Arblaster, 2002b; Rajendran et al., 2004). Most coupled GCMs have too much precipitation over the Indian Ocean and less over the Indian subcontinent during northern summer. Finally, atmospheric and coupled GCMs are more successful at reproducing the broad-scale features of the ISM circulation than regional features like the strength of the Somali Jet or ISM rainfall over the Indian subcontinent (Sperber and Palmer, 1996; Meehl and Arblaster, 1998; Cherchi and Navarra, 2002).

Simulating the annual cycle and El Niño-like phenomena in the Pacific also remains a difficult task for recent coupled GCMs (Latif et al., 2001; Davey et al., 2002; AchutaRao and Sperber, 2002). Many of these have a double ITCZ for much of the year in the Pacific and a semiannual component in equatorial SST and zonal wind stress which is much stronger than in observations. The correct simulation of ENSO appears to be sensitive to the skill of the simulated seasonal cycle over the equatorial Pacific (AchutaRao and Sperber, 2002).

Finally, coupled or hybrid GCMs also have difficulty in simulating ENSO-ISM relationships (Kirtman and Zebiak, 1997). ISM rainfall and dynamical indices show an inverse relationship with Niño3 SST in coupled models—weak monsoons are generally associated with Niño-like conditions in the eastern Pacific (Meehl and Arblaster, 1998; Kitoh et al. 1999). However, very few coupled GCM studies show a strong impact of anomalous monsoons on La Niña or El Niño events in the Pacific, in contradiction with observational studies.

In this study, we present a detailed investigation of ISM-ENSO relationships both from observations and a coupled GCM simulation. The major focus of this study is to document the ability of this state-of-the-art CGCM to reproduce the observed lead-lag relationships between the ISM and ENSO, and to understand how systematic errors may affect the simulation of these relationships. The coupled GCM used in this paper is the SINTEX model (Gualdi et al., 2003a). The mean state and seasonality of the tropical climate simulated by the SINTEX model has been the subject of a previous paper (Gualdi et al., 2003a). Moreover, this coupled GCM has been shown to reproduce many features associated with ENSO and Indian Ocean variability (Guilyardi et al., 2003; Gualdi et al., 2003b). Here, we focus mainly on the links between ENSO and the ISM on the interannual time scale.

The following Section 2 describes the coupled model, as well as validation data and the methods used in this study. Salient features of the seasonal cycle of the coupled GCM are discussed in Section 3 since this is a prerequisite for a correct simulation of ISM-ENSO relationships. The simulated interannual variability and the ENSO-ISM relationships are compared with observations in Section 4. The conclusions follow in Section 5.

2. The coupled model, validation data and methods

a. The coupled model

The model used for this study is the ECHAM-ORCA coupled GCM developed within the SINTEX (Scale INTeraction EXperiment) EU project, and is described in detail in Gualdi et al. (2003a). ORCA is the global version of the OPA 8.1 ocean modeling system developed by the LODYC team in Paris (Madec et al. 1998, see full documentation at http://www.lodyc.jussieu.fr/opa/). Its space resolution is roughly equivalent to a geographical mesh of 2 by 1.5 ° (with a meridional resolution of 0.5 ° near the equator). There are 31 vertical levels with 10 levels in the top 100 meters. There is no interactive sea-ice model in the configuration used for the present study; sea-ice cover is relaxed towards the observed monthly climatology. ECHAM-4 is the fourth generation of the ECHAM atmospheric GCM developed at the Max Planck Institut Für Meteorologie in Hamburg. An exhaustive description of the dynamical and physical structures, as well as the simulated climatology of ECHAM-4 may be found in Roeckner et al. (1996). Here, ECHAM-4 is run at T30 spectral resolution, corresponding to a horizontal resolution of about 3.75°, with 19 vertical layers (the highest at 10 hPa). The parameterization of convection is based on the mass flux concept, where cumulus clouds are represented by a bulk model including the effects of entrainment and detrainment on the updraft and downdraft convective mass fluxes (Tiedtke, 1989).

ORCA and ECHAM-4 are coupled through OASIS 2.4 (Valcke et al. 2000). From Levitus (1982), the model is integrated for 2 years in ocean robust-diagnostic mode. Once the ocean dynamic is spun-up, the integration continues without any adjustment or restoring (except in regions where sea-ice cover does not agree with climatology). Air-sea fluxes and the SST are exchanged every 3 hours. The simulation analyzed in this study was integrated for 200 years.

b. Data

We use the NCEP/NCAR reanalysis from 1948 to 1998 (Kalnay et al., 1996), the Empirical Orthogonal Function (EOF) reconstructed SST analysis of Smith et al. (1996) from 1950 to 1998 (hereafter referred to as Reynolds SST) and the Climate Prediction Center Merged Analysis of Precipitation (CMAP) from January 1979 to December 1999 (Xie and Arkin, 1997) in order to validate the outputs from the SINTEX model. Various ENSO indices (SST Niño12 [0-10°S,90°-80°W], Niño3 [5°N-5°S,150°-90°W], Niño34 [5°N-5°S,170°E-120°W], Niño4 [5°N-5°S,160°E-150°W] indices, SLP Darwin and Tahiti time series) are adapted from the Climate Prediction Center (CPC). Finally, the area weighted monthly rainfall series for all India (IMR) has also been used to document ISM rainfall variability over the Indian subcontinent (Parthasarathy et al., 1995). The IMR series is available for the period 1871-1998 and is constructed from observations of land-based rain gauge data.

c. Methods

Composite and correlation analyses have been performed to highlight the space-time structure of Indo-Pacific variability. Special attention has been paid in assessing the significance of the composite anomalies with the method explained in Terray et al. (2003). Wavelet analysis (Torrence and Compo, 1998) has been used to reveal the temporal structure of the various time series, since it is expected that most of these time series will be nonstationary.

3. The Indo-Pacific annual cycle

In this section, we describe the annual cycle in rainfall, pressure vertical velocity, surface and upper-level winds in the Indian and Pacific Oceans. For each of the variables, monthly means are computed from the longest period available for both the observations and the simulation.

a. Indian Ocean

The July and January climatologies of 850 hPa wind and 500 hPa pressure vertical velocity in the Indo-Pacific areas are shown in Fig. 1 for the reanalysis and the simulation. The 200 hPa wind and Sea Level Pressure (SLP) climatologies are displayed in Fig. 2.

The SINTEX model qualitatively represents many aspects of the observed wind field during northern summer (Fig. 1). The cross-equatorial flow at 850 hPa is in agreement with the NCEP reanalysis, with strong southwesterly inflow into south Asia from the Arabian Sea and Bay of Bengal. However, upward vertical velocity is observed just north of the equator in the Arabian Sea, and the Somali Jet is therefore not confined near the African coast. In the Arabian Sea, the monsoon flow is too zonal. The monsoon trough is also not very marked in the simulation. At 200 hPa, the most outstanding feature in northern summer is a huge anticyclonic circulation, the Tibetan high, centered over the southern part of the Tibetan Plateau (Fig. 2a). At this level, the cross-equatorial flow is mainly concentrated along the south east periphery of the Tibetan high and northeasterly winds prevail over the south Asian region. Easterly upper-level winds also prevail over the North Indian Ocean in the simulation, but are lower in magnitude relative to those observed (Fig. 2b).

During the winter monsoon, the general flow over the region is reversed. The northeasterly trades of the Northern Hemisphere cross the equator mainly off the African coast and move eastward towards the convection center located over Indonesia and Australia (Fig. 1c). The SINTEX model qualitatively represents most major features of the winter climatology (Fig. 1d). However, due to stronger-than-observed northerly flow along the Somali coast, the South Indian Ocean ITCZ is located in the central Indian Ocean. This westward displacement of the ITCZ is associated with warmer-than-observed SST in the western Indian Ocean (not shown). The reversal of upper-level winds with season is simulated realistically in the SINTEX model (Figs. 2c, d). However, westerly winds are stronger than observed during northern winter over Peninsular India. All these features suggest that the winter Asian monsoon is too strong in the simulation.

The July and January precipitation climatologies are shown on Fig. 3. During the ISM, abundant precipitation is observed along the west coast of India with values exceeding 18 mm/day, accompanied by a strong east-west gradient with values less than 4 mm/day along the east coast. Other important aspects of the spatial distribution of ISM rainfall over land are the small amounts over the north western deserts and the belt of heavy precipitation associated with the monsoon trough along the Gangetic plains. Over the Indian Ocean, striking features are the presence of a belt of heavy rainfall just south of the Equator between 70°E and 100°E and large precipitation amounts over the bay of Bengal anchored to the west coast of Myanmar (Fig. 3a). The model simulates a local precipitation maximum over the Arabian Sea during July and August, which are not observed, and fails to reproduce the heavy rainfall along the west coast of India and Myanmar (Fig. 3b). However, a gradient in monsoon rainfall from the West Coast towards the east is simulated as is observed (Fig. 3b). The sharp contrast in the ISM precipitation from the northwestern desert areas to the wet Gangetic plains is well reproduced by the model (Fig. 3b). During boreal winter, the SINTEX model qualitatively reproduces the regional rainfall pattern, with the greatest rainfall south of the equator. However, more precipitation than observed is simulated in the western Indian Ocean. This bias is clearly associated with the westward displacement of the ITCZ in the simulation relative to the observations (Figs. 1c, d).

Fig. 4 shows the annual cycle of the simulated and observed IMR indices. In the simulation, IMR is defined as the area-averaged precipitation over all land grid-points in the domain 75°E-85°E, 10°N-25°N. The model simulates a reasonable annual cycle with the summer precipitation maximum in the Indian areas as in observed climate. One of the major deficiencies of the simulated ISM is that precipitation amounts are much less than observed during all the monsoon months (June-September). Finally, during fall and winter greater precipitation over the Indian subcontinent is simulated relative to that observed.

We now focus on the annual cycle of the Walker and Hadley circulations over the Indian Ocean. Fig. 5 shows the climatology of surface and upper-level winds area-averaged over the Extented Indian Monsoon Rainfall (70°E-110°E, 5°N-30°N, hereafter EIMR) and EQuatorial Indian Ocean (60°E-90°E and 2.5°S-2.5°N, hereafter EQIO) areas for both the simulation and the reanalysis. A strong vertical shear with strong upper-level easterlies overlying surface westerlies (Figs. 5a, b), and a meridional circulation with low-level poleward flow and upper-level equatorward flows (Figs. 5c, d) are noted over the North Indian Ocean during the ISM. Interestingly, over the equatorial Indian Ocean, upper-level easterlies are observed year round, but the zonal wind speed dramatically decreases from 22 m/s in July to 8 m/s in January (Fig. 5.e). This suggests that the equatorial upper-level easterlies are strongly enhanced by ISM convection during northern summer. This becomes evident when comparing the annual cycle of 200 hPa zonal wind over the equatorial Indian Ocean with the rainfall and pressure vertical velocity annual cycles (Figs. 1 and 3). The latent heat release associated with the Asian monsoon is much stronger than its counterpart in the South Indian Ocean during austral summer. As a consequence, the upper branch of the related Hadley circulation is strengthened. Furthermore, the active convection center is located far away from the equator during the ISM and the Coriolis acceleration is quite effective in accelerating the associated upper-level northeasterlies. In other words, the upper-level equatorial easterlies observed during the ISM are closely associated with the upper branch of the local Hadley circulation. All these features are apparent in the simulation with the correct seasonal phasing, but with considerably weaker amplitude. The weakening of the whole ISM circulation and more specifically of the local Hadley cell in the model experiment appears to play a crucial role in determining the precipitation biases during northern summer. On the contrary, the stronger-than-observed surface and upper-level flows during northern winter are symptomatic of the strengthening of the Asian winter monsoon in the simulation. Finally, the model is not able to capture the semi-annual cycle of the surface zonal wind over the equatorial Indian Ocean. This bias is linked to the incorrect location of the ITCZ in the central

Indian Ocean and the erroneous extension of the Southern hemisphere trade winds into the eastern Indian Ocean north of the equator during boreal fall (see Fischer et al., 2003).

b. Pacific Ocean

Salient features of the SINTEX model in simulating the Pacific annual cycle are described here and are more fully described in Gualdi et al. (2003a) and Guilyardi et al. (2003).

During northern summer, the SINTEX model captures the observed pattern in the tropical Pacific with wet conditions north of the equator and dry conditions in the eastern Pacific (Fig. 3). The western north Pacific ITCZ, as estimated from the CMAP dataset, (the so-called Western North Pacific Summer Monsoon, WNPSM hereafter) has its center located over the domain (10°-20°N, 130°-150°E), collocated with the warm pool in the western Pacific. This updraft center is shifted 30° to the east in the simulation, where a local minimum in the northern ITCZ is found in the CMAP dataset (Fig. 3). This error may be related to the anomalous strength of the subtropical highs in the Pacific (Figs. 1 and 2) and the associated extent of the equatorial cold tongue too far west into the warm pool area. This displacement of the rain band toward the central Pacific is also associated with SST errors in this region (not shown). Moreover, this rainfall band is too zonally oriented and is sandwiched between the too strong low-level anticyclonic flow associated with the North and South Pacific subtropical highs. Undoubtedly, rainfall in the central Pacific north of the equator is largely enhanced by the stronger-than-observed convergence between the trade winds of the two hemispheres in the simulation. This systematic error in the location of the WNPSM has a pronounced effect on the structure of the Walker cell over the equatorial Pacific. During boreal summer, the surface wind has a strong northward component over the central equatorial Pacific in the simulation, but is nearly zonal in the reanalysis. Moreover, Fig. 2b reveals the establishment of a westerly duct that stretches across the central North and South Pacific at 200 hPa in the simulation. This feature is absent in the reanalysis (Fig. 2a). In other words, Figs. 1b and 2b indicate the organization of a vigorous circulation cell between the shifted WNPSM and the South Pacific subtropical high in the simulation.

During northern winter and spring, the South Pacific Convergence Zone (SPCZ) is too zonally oriented and extends too far east in the simulation (Fig. 3). Due to this unrealistic southern ITCZ, another atmospheric cell linking the SPCZ and the North Pacific subtropical high emerges during northern winter in the simulation. During this season, the meridional component of the lower and upper-level winds is rather weak in the reanalysis. In contrast, both the lower and upper-level winds over the western Pacific have a significant meridional component in the simulation, related to the erroneous SPCZ during northern winter.

The SST annual cycle of the coupled model is characterized by an eroded warm pool and a year-round too-deep thermocline in the central Pacific, as found in many other coupled models without flux adjustments (Fig. 6; Guilyardi et al., 2003). These well-known and poorly-understood errors are linked to a stronger-than-observed zonal wind west of the dateline extending into the West Pacific warm pool (Fig. 1). The SST annual cycle in the eastern equatorial Pacific is substantially reduced. In the central Pacific, the annual cycle has an incorrect semiannual component with a secondary minimum in January-December when the observed SST reaches its maximum. This semiannual cycle is also evident in the western Pacific where it is more pronounced than in observations.

Specific circulation patterns are linked to the SST equatorial distribution. Fig. 7 shows the annual cycle of the surface and upper-level zonal wind in the central EQuatorial PACific (160°W-130°W, 2.5°N-2.5°S; hereafter EQPAC) for the simulation and the reanalysis, in order to examine the annual cycle of the Walker circulation across the Pacific. The zonal surface wind speed maxima in the central equatorial Pacific occur twice a year when the SST gradient along the equator is maximum (Fig. 6). Thus, the systematic phase change in the annual cycle of surface zonal wind is significantly correlated with the annual cycle in SST, suggesting the role of air-sea interactions on the annual time scale. The phase of the surface zonal wind is correct in the simulation, but has a stronger semiannual component and a reduced amplitude. Interestingly, the strength of the equatorial upper-level westerlies is not correlated with the intensity of the surface flow in the reanalysis. As an example, the speed of the upper-level westerlies over the EQPAC area is near zero when a maximum of surface easterlies appears during the ISM. Conversely, maxima of both the surface easterlies and upper-level westerlies are observed during northern winter. Linear models (Gill, 1980; Young, 1987) provide some guidance in explaining these points. During northern winter, the convection center in the Indo-Pacific region is located in the vicinity of the equator and may be considered as a symmetric heat source (Fig. 3). As a consequence, a Kelvin wave is generated to the east of the forcing with strong upper-level westerlies and the establishment of a thermally direct east-west circulation in the equatorial plane (Gill, 1980). On the other hand, the convection center is located at about 15° during northern summer and may be interpreted as an asymmetric heat source (Fig. 3). In this case, the atmospheric response is restricted to Rossby waves to the west of the updraft center (Young, 1987). Even though these considerations apply only to the divergent part of the upper-level wind field, they may partly explain why the strength of the surface easterlies and upper-level westerlies over the equatorial Pacific are essentially uncorrelated during northern summer. In the model experiment, the annual cycle of the upper-level zonal wind is structured by a strong semiannual component, in total disagreement with observations, and prominent upper-level westerlies are simulated over the equatorial central Pacific during the ISM. It is reasonable to attribute this semiannual component of the simulated upper-level zonal wind over the central Pacific to the upper branch of the erroneous cell linking the shifted WNPSM and the South Pacific subtropical high in the simulation during boreal summer.

c. Summary

In this section, some of the characteristic features of the annual cycle in the tropics have been investigated. One major finding with respect to monsoon-ENSO relationships is that the upper-level easterlies over the equatorial Indian Ocean are largely controlled by the latent heat release associated with the Asian monsoon. Another is that the relative dissociation on the annual time scale between the upper-level equatorial westerlies over the Pacific and the active convection center north of the equator during northern summer. The SINTEX model captures some aspects of this complex Indo-Pacific annual cycle, but not all. In particular, the ISM is realistically simulated, but is weak relative to the NCEP reanalysis. The SINTEX model also has difficulties in simulating the seasonal cycle in the tropical Pacific, and has a tendency to produce a double ITCZ, like many other coupled models (Davey et al., 2002; AchutaRao and Sperber, 2002).

SST, precipitation and wind errors in the tropical Pacific annual cycle are closely tied through coupled feedbacks. The stronger-than-observed trade winds over the Pacific associated with the abnormal strength of the North and South subtropical highs lead to the extension of the eastern equatorial Pacific cold tongue regime too far westward into the warm pool. As a consequence, drier-than-observed conditions are simulated in the western Pacific and the WNPSM is shifted eastward near the dateline during northern summer. These errors contribute, in turn, to a strong and erroneous semiannual component in the simulated Pacific Walker circulation. In the following sections, we will investigate whether we can use these biases to get a better understanding about the connection between both oceans. What influence does the erroneous Pacific annual cycle have on the Indo-Pacific interannual variability? To what extent do these biases influence the monsoon-ENSO relationships in the coupled simulation?

4. Indo-Pacific interannual variability

a. Indian Summer Monsoon

Our attention is first focused on ISM interannual variability as summarized by the behaviour of monsoon rainfall and circulation indices. The standard deviations of the observed and simulated IMR indices are 83 and 92 mm respectively. Thus, the simulated amplitude of ISM variability compares favorably with observations. The results of the wavelet analysis from the observed and simulated IMR indices are very similar (Figure not shown). Both IMR indices have an intermittent oscillation around 2-3 years which is significant at the 90% confidence level against a white noise wavelet spectrum. The observed and simulated quasi-biennial oscillations exhibit a considerable amplitude modulation. Both series are also structured with longer oscillations around 64 and 128 years. However, these periodicities are affected by "edge" effects in the wavelet analysis.

Following Wang and Fan (1999), we have defined several dynamical monsoon indices in order to evaluate the simulated ISM circulation. Similar indices have been defined from the NCEP reanalysis for the period 1948-1998:

- The Indian Ocean Walker (IOW) index is defined as the difference between the standardized zonal wind anomalies at 850 hPa and 200 hPa area-averaged over the EQIO area. This time series represent the interannual variability of the equatorial east-west circulation over the Indian Ocean (Hastenrath, 2000).
- The Indian Ocean meridional wind Shear (IOVS) index is defined as the difference between the standardized meridional wind anomalies at 850 hPa and 200 hPa area-averaged over the EIMR region. This IOVS index is similar to the vertical meridional shear index proposed by Goswami et al. (1999), except that the monthly 850 hPa and 200 hPa zonal wind time series have been standardized before computing the difference. Since the variance of the wind is much higher at 200 hPa this is a necessary step if we want to give the same weight to the two time series in the IOVS index.
- The Indian Ocean zonal wind Shear (IOUS) index is defined as the difference between the standardized zonal wind anomalies at 850 hPa and 200 hPa area-averaged over the EIMR region. This time series is similar to the vertical zonal wind shear index proposed by Webster and Yang (1992), except for the standardization.

Tables 1 and 2 present the cross-correlations between the various precipitation and dynamical ISM indices for the observations and the simulation, respectively. A rainfall index associated with the WNPSM has also been included in order to investigate the links between the rainfall variability over the western Pacific warm pool area and the ISM. Moreover, the consideration of this index is of paramount importance in assessing the monsoon-ENSO relationships, since the wind anomalies over this area were shown to play active roles in the turnabout of ENSO in both observations (Wang et al., 1999) and the SINTEX simulation (Guilyardi et al., 2003). This time series is defined as the area-averaged precipitation over the region 10°-20°N and 120°-150°E during June-September both for the CMAP dataset and the simulation. For the ISM, the results from the reanalysis and the simulation are broadly consistent. The cross-correlation between the IMR and IOVS indices are high and significant whereas IMR is weakly correlated with IOUS. The correlations of the IMR indice with the zonal and meridional wind components at 200 and 850 hPa confirm that the meridional wind shear over South Asia is strongly related to ISM rainfall in both observations and the simulation. On the contrary, the role of the zonal wind shear is very modest as far as ISM rainfall variability is concerned. A wavelet analysis of the summer IOVS indices for observations and the simulation shows a concentration of energy at the quasi-biennial time scale (not shown). This dynamical index is thus structured by the same periodicities as the IMR index, suggesting again that ISM rainfall variability is largely controlled by the monsoon Hadley circulation in both the simulation and the reanalysis. These results agree with the observational study of Goswami et al. (1999) which suggests that interannual variability of ISM rainfall is strongly associated with the strength of the (inverse) Hadley cell over South Asia. Processes other than the latent heat release over the Indian subcontinent and adjacent oceanic areas may contribute to the fluctuations of the IOUS index.

In contrast, the relationships between WNPSM interannual variability and the dynamical indices are not captured in the simulation. In the observations, the WNPSM rainfall index is significantly correlated with the IOUS index (0.72), but fluctuates independently of the IOVS index (-0.19). We also note that the correlation between the ISM and WNPSM rainfall indices is negligibly small (-0.06) during 1979-1998. Thus, the ISM and WNPSM systems may be considered to be nearly independent convective centers in the observations, at least in a statistical sense. These results corroborate the findings of Ailikun and Yasunari (2001) and Wang et al. (2001). On the contrary, the WNPSM rainfall index is significantly and negatively correlated with both the ISM rainfall and IOVS indices in the simulation (-0.37 and –0.38, respectively). This significant negative correlation between the ISM and WNPSM rainfall indices suggests that the ISM and WNPSM convective centers are systematically out of phase in the model experiment. Moreover, the correlation between the WNPSM rainfall and IOUS indices is quite modest (0.26) and not even physically consistent when considering the 850 and 200 hPa zonal wind anomalies used to construct the IOUS index.

In the context of monsoon-ENSO relationships, it is important to keep in mind the significant correlation of the ISM and WNPSM indices, in the reanalysis, with the strength of the 200 hPa easterlies over the Indian Ocean during northern summer. Both updraft centers may contribute independently to the strength of the upper-level easterlies at 200 hPa over the central Indian Ocean. The coupled model is only partially successful in simulating these features, particularly for the WNPSM. The correlation of the summer 200 hPa easterlies over the equatorial Indian Ocean with the ISM and WNPSM rainfall indices suggests that the latent heat release associated with these two updraft centers have, in the simulation, opposite effects on the upper-level wind over the equatorial Indian ocean contrary to the observations.

b. Pacific Ocean

We first compute standard deviations of monthly SST anomalies in the Niño12, Niño3, Niño34 and Niño4 regions as a simple measure of ENSO amplitude and structure in the simulation and observations (Table 3). The SINTEX model is producing roughly 50-60% the amplitude of the observations for the period 1950-2000. However, Gualdi et al. (2003a) have shown that significant temporal changes in the standard deviation of Niño3 SST anomalies exist in the SINTEX simulation as in observational data. Thus, the model reproduces some features of the observed low-frequency variability associated with ENSO. Standard deviations in Table 3 also suggest minimum variance over the western Pacific, with maximum in the eastern portion of the basin as the observed. Very few coupled models capture this variability pattern across the equatorial Pacific (AchutaRao and Sperber, 2002). Monthly standard deviations for the Niño34 time series vary from 0.6°C (in April) to 1.2°C (in December) for the observations and from 0.38°C (in March) to 0.53°C (in December) for the SINTEX model. In other words, the model is able to simulate the seasonal phase locking of the Niño34 variability, with greater monthly standard deviations in boreal winter, decreased in boreal spring, even though the amplitude of the annual cycle is considerably reduced. Another useful index is the Southern Oscillation Index (SOI) which characterizes the global scale seesaw in surface pressures associated with ENSO (Trenberth and Caron, 2000). Using monthly anomalies with the annual cycle removed, the cross-correlation between Darwin and Tahiti SLP time series is –0.36 during 1950-2000. In the model experiment, the SOI may be computed from the SLP difference of the grid points corresponding to Tahiti and Darwin. However, the correlation between these two time series is 0.18 indicating that the model is not able to locate one or both centers of action of the SO. The correlation of Darwin SLP monthly anomalies with Niño34 SST anomalies is 0.66 and 0.33 for observations and the simulation, respectively. On the other hand, the correlation of Tahiti SLP monthly anomalies with Niño34 SST anomalies is –0.52 and 0 for observations and the simulation, respectively. Tahiti is under the influence of the Southern ITCZ year round in the simulation due to the systematic errors discussed in section 3. The SOI is one of the basic indices used to validate ENSO variability in coupled models (AchutaRao and Sperber, 2002). However, our analysis demonstrates that for coupled GCMs affected by the SPCZ bias, this time series is not a measure of the large-scale seesaw in SLPs associated with ENSO.

The wavelet spectrum of the observed Niño34 has a broad peak at a 2-6 year time scale, significant at the 95% confidence level assuming a red noise background spectrum (not shown). The broadness of the peak suggests that the ENSO phenomenon has an irregular period over time and that the Niño34 SST time series is red in character apart from the annual cycle. The model captures this irregular periodicity of the Niño34 index even though the significant periodicities are now at higher frequencies, between 1.8 and 4 years, and are more concentrated (not shown).

c. El Niño-Monsoon relationships

1) Analysis of the ISM response during El Niño

As described in Guilyardi et al. (2003), the SINTEX model exhibits two types of El Niño events. Regular El Niño events, which start in May and peak in December, and aborted El Niño events with a short life cycle, which peak in May and reach a cold state one year later (See figure 6 of Guilyardi et al., 2003). Since El Niño events are phase-locked with the annual cycle in both observations and the simulation, we adopt a composite approach in analyzing the typical ISM response for El Niño events. Regular El Niño events are defined in terms of winter (December-February) Niño34 SST exceeding 1 standard deviation in the simulation. During the 200 years of the simulation, there are 37 regular El Niño years. Aborted El Niño events are defined in terms of spring (April-June) Niño34 SST exceeding 1 standard deviation and winter (December-February) Niño34 SST between –0.5 and 0.5 standard deviation. Seventeen aborted El Niño years have been identified in the simulation. Following the lists of El Niño events compiled by Trenberth (1997), we select the 13 El Niño events that occurred at the end of the years 1951, 1953, 1957, 1963, 1965, 1968, 1972, 1976, 1979, 1982, 1986, 1991, 1997 in the observations. As aborted El Niño events are rarely observed, there is no aborted El Niño composite for the observations. Tables 4 and 5 present composite standardized anomalies and statistics of ISM rainfall and dynamical indices for the El Niño events extracted from the observations and the simulation, respectively. The SINTEX model reproduces the observed ENSO-related ISM rainfall and atmospheric variability reasonably well (Tables 4, 5). El Niño years are associated with significant negative rainfall anomalies over the Indian subcontinent in both the simulation and the observations. However, the ISM-ENSO relationship is far from rigorous in both cases, since some El Niño events are associated with positive ISM rainfall anomalies, as indicated by the MAX indicator given in Tables 4 and 5. Interestingly, El Niño years are associated with a weakened Hadley circulation over the Indian Ocean. Meanwhile, the 850 and 200 hPa zonal wind anomalies averaged over the EIMR region have the same sign during El Niño years in both the simulation and observations (Tables 4 and 5). This result implies again that the IOUS index is not a good indicator for ISM variability, even in the context of ENSO-monsoon relationships. The composite analysis from the observations clearly suggests that the remote influence of ENSO on ISM variability is through the upper-level zonal fields over the Indian subcontinent and equatorial Indian Ocean, since all the 200 hPa zonal wind indices have anomalies significant at the 1% confidence level. This relationship is well reproduced by the aborted but not by the regular El Niño events in the simulation. None of the 200 hPa zonal wind indices are significant even though they have the correct sign for regular El Niño events. Overall, the statistics for the observations are in closer agreement with the aborted El Niño statistics than the regular ones in the simulation. However, we will not consider aborted El Niño events in the rest of this section as they are not frequently observed.

To more precisely illustrate the atmospheric response to regular El Niño events, the May-September monthly composites of the 850 hPa wind and 500 hPa vertical pressure velocity are shown in Fig. 8. These composite maps are masked to exhibit only wind anomalies that exceed the 10% confidence level, and we only discuss the features that are significant at this level. In the Pacific, the 850 hPa wind anomalies show the dramatic perturbation of the Pacific Walker circulation associated with (regular) El Niño events both in observations and the simulation. However, the wind and pressure vertical velocity anomaly patterns over the Pacific are not very consistent between the observations and the simulation (Fig. 8). The ENSO-related equatorial wind and pressure vertical velocity anomalies are systematically shifted 40° to the west during regular El Niño events in the simulation. This is symptomatic of the westward extension of the cold tongue regime into the Pacific warm pool area discussed in section 3. The simulated equatorial wind anomalies between 160°E and 130°W have also a much-too-strong north-south component (Fig. 8). This suggests interannual fluctuations of the erroneous circulation cell that develops between the shifted WNPSM and the South Pacific subtropical high in the simulation (section 3). Finally, a significant cyclonic circulation develops off the east coast of Asia during July and August in the simulation which is not seen in the observations. These discrepancies are clearly linked to systematic errors in the simulation of the Pacific annual cycle and more specifically to the displacement of convective centers and the too-elongated SPCZ in the simulation.

The monsoon circulation anomalies associated with ENSO are either driven remotely by teleconnections through changes in the Walker circulation, or locally by anomalous heating or air-sea interactions (Ju and Slingo, 1995). In the NCEP reanalysis, the May-June composites suggest that the ISM dynamics are strongly influenced by anomalous subsidence over Indonesia and the western North Pacific induced by the modulation of the Walker circulation and changes in heating patterns over these regions. The main influence of ENSO appears to be a reduced monsoon flow with northerly wind anomalies along the Somali coast and easterly wind anomalies north of the equator during May and June. These features suggest a delayed ISM onset during El Niño years (Joseph et al., 1994). This relationship does not exist in the simulation, as no significant wind anomalies are seen in May-June of the model composites. This is probably due to the westward extension of the cold tongue regime into the Pacific warm pool. However, El Niño years are associated with downward 500 hPa pressure vertical velocity anomalies over the Indian subcontinent in both the simulation and the observations, during the whole summer (Fig. 8). The El Niño 850 hPa wind composites also reflect the lower-tropospheric vorticity anomalies associated with the weakening of the ISM trough during September in both cases (Fig. 8). Other important features observed during El Niño years are a weakened Mascarene high and a reduced Somali jet during most summer months in both observations and the simulation. Interestingly, significant downward pressure vertical anomalies are also observed over the maritime continent and in the south-east tropical Indian Ocean from June to September of El Niño years in both cases. These anomalies are collocated with significant southeasterly wind anomalies off the west coast of Sumatra. The wind-thermocline-SST feedback which is very active off the west coast of Sumatra during boreal summer (Gualdi et al., 2003b; Wang et al., 2003; Li et al., 2003) may explain the growth of the anomalous anticyclone in this region. However, this positive feedback is much more active in the simulation due to a shallower-than-observed thermocline along Sumatra during late summer and fall (Fischer et al., 2003). This systematic model bias is also linked to the westward extension of the Pacific regime into the eastern Indian Ocean discussed above. This bias favors easterly rather than westerly climatological wind in the eastern equatorial Indian Ocean during late summer and fall in the simulation (Fischer et al., 2003, their Fig. 2). The stronger-than-observed anomalous anticyclone in the southeast Indian Ocean is associated with a vigorous anticlockwise circulation centered over the equatorial Indian Ocean during late summer in the simulation, which is not really seen in observations (Fig. 8). This anomalous circulation pattern strongly influences the ISM by weakening the Somali jet and the low-level westerlies over the Arabian Sea during the late summer in the simulation. In the reanalysis, these relationships are only partially observed during September.

2) The lead-lag relationship between ENSO and ISM anomalies

A challenging test of a coupled model is reproduction of the observed lead-lag relationships between ENSO and ISM. Figs. 9.a,b show the lead-lag correlations between monthly Niño34 SST and the ISM rainfall time series for the recent 128 year period and the 200 years of the simulation. Relatively cold (warm) Niño34 SSTs are associated with strong (weak) monsoons during boreal summer (Fig. 9.a). This relationship grows consistently, from spring through the entire development of ENSO, until the end of the year. Strong (weak) ISMs develop during onset and maturing stages of La Niña (El Niño) events (Wang et al., 2001). The highest negative correlations are noted during the late ISM and the following months in the observations (Fig. 9.a). This led some authors (Yasunari, 1990; Kirtman and Shukla, 2000) to suggest that anomalous monsoons provide favorable conditions for triggering or enhancing cold/warm events in the Pacific during the following winter, while others (Goswami and Jayavelu, 2001) interpret these lead-lag relationships as a passive response of the ISM to ENSO, with the higher correlations occurring at the end of the year because ENSO events are phase-locked to the annual cycle and peak at the end of the year. However, the more striking feature of Fig. 9.b is that the SINTEX model does not capture the observed lead-lag relationships between ENSO and the ISM. Starting six months before the ISM, the correlation between Niño34 SSTs and ISM rainfall is already negative and significant (Fig. 9.b). The amplitude of this negative correlation increases until the early ISM (June and July) and fades away very rapidly during the late ISM and the following months in the simulation (Fig. 9.b). Moreover, the magnitude of the correlations is weak in the simulation compared to the observations. Similar results are obtained with Darwin SLP time series taken as an ENSO index (not shown). The significant correlations prior to the ISM in the simulation are very intriguing and have been investigated in more detail. As noted above, ISM variability is significantly associated with both regular and aborted ENSO events in the simulation (Table 5). Since aborted El Niño (La Niña) events peak in May-June and reach a cold (warm) state at the end of the year (Guilyardi et al., 2003, their figure 6), it is possible that the lead-lag relationships between ISM and Niño34 SSTs are contaminated by aborted ENSO events in the simulation. In order to test this possibility, the aborted ENSO years (17 El Niño and 15 La Niña years) have been excluded from the lead-lag correlation analysis in Fig. 9.c. The negative correlations prior to the ISM, though still negative, have been significantly reduced by the exclusion of aborted ENSO events. However, the overall lead-lag relationships between ISM and Niño34 SSTs are rather similar, suggesting that other factors also contribute to this systematic bias in the simulation.

3) Analysis of ENSO and tropical western Pacific variability during anomalous ISMs

Possible other reasons for this shortcoming of the SINTEX model are now examined with the help of a composite analysis of the surface wind and SST fields, based on the IMR index. Classification of a weak (strong) ISM year is made when the standardized IMR is < -1 (> 1). Using this criterion, there are 8 strong and 11 weak ISMs during the 1948-1998 period. 32 strong and 34 weak ISM years are selected in the simulation with the same definition. The strong (weak) ISM years corresponding to aborted La Niña (El Niño) years were excluded from the composite analysis in order to identify other factors which may contribute to the lead-lag relationships between ISM and Niño34 SSTs in the simulation. This leaves 28 strong ISM years and 27 weak ISM years in the composites from the simulation.

Figure 10 shows the June-July and August-September composite 850 hPa wind and 500 hPa pressure vertical velocity anomalies over the Indian and Pacific oceans during weak ISMs. Again, we discuss features that are significant to at least to the 10% confidence level. In the reanalysis (Figs. 10.a, c), the surface wind anomaly pattern over the Indian Ocean corresponds to a weakening of the low-level circulation that is typical of weak ISM years (Annamalai et al., 1999; Wang et al., 2001, Terray et al., 2003). Weak ISMs are associated with a weakened Somali Jet, easterly wind anomalies over the Arabian Sea, and westerly wind anomalies over northwest India. This wind pattern is consistent with the reduced monsoon trough over India as indicated by downward 500 hPa pressure vertical velocity anomalies over India. Downward pressure vertical velocity anomalies are also observed over Borneo, Indonesia and New Guinea (Figs. 10.a, c), as in the El Niño composites (Fig. 8). At 200 hPa, the dominant features are a weakening of the tropical easterly jet and pronounced eastward propagation of westerly anomalies over the whole Indian Ocean (figure not shown). The potential influence of the ISM on the coupled ocean-atmosphere system in the Pacific Ocean is also illustrated in Figs. 10.a, c. Significant westerly wind in the low troposphere, and upward pressure vertical velocity anomalies are observed over the central equatorial Pacific between 180°-130°W during weak ISMs. Over the central and eastern Pacific, the climatological surface flow is easterly near the surface (section 3). Consequently, the preceding result indicates that a weakening of the Pacific trade winds occurs during weak ISMs in the reanalysis. Moreover, the surface wind anomaly patterns over the north and south Pacific suggest that the Pacific subtropical highs are also weakened during weak ISMs. However, since many weak ISM years are also El Niño years, these significant surface wind anomalies in the Pacific may be associated with a developing El Niño event and are not necessarily the signature of the ISM (Goswami and Jayavelu, 2001). The coupled model realistically simulates the atmospheric response to weak ISMs over the Indian subcontinent and western Indian Ocean (Figs. 10.b, d). On the other hand, there is considerable disagreement between the observed and simulated Pacific and eastern Indian Ocean variability during weak ISMs. Significant surface westerly wind anomalies over the Pacific are restricted to the western Pacific during weak ISMs in the simulation (Figs. 10.b, d). Moreover, these westerly wind anomalies are associated with anomalous ascent over the western North Pacific and a huge anomalous cyclonic circulation that develops off the east coast of Asia during June-July. This is in agreement with the significant negative correlation between ISM and WNPSM rainfall indices in the simulation, but is in contradiction with observations (Figs. 10.a, c). No significant zonal wind anomalies are observed east of the date line over the equatorial Pacific in the simulation, even though such wind anomalies are observed in the El Niño composites (Fig. 8). Composite analysis with respect to strong ISMs in the reanalysis shows reversed surface atmospheric anomaly patterns in Indo-Pacific areas (Figs. 11.a, c). However, significant easterly wind anomalies over the central equatorial Pacific are only observed during the late ISM (August and September). The tropical response to strong ISMs is generally well-portrayed in the simulation, including the strengthening of the climatological easterlies over the central equatorial Pacific during the late summer (Figs. 11.b, d). The main discrepancy is again the significant out-of-phase relationship between anomalous ascent over India and anomalous subsidence over the western North Pacific during the entire summer in the simulation (Figs. 11.b, d), not seen in the observations (Figs. 11.a, c).

The February-March and April-May SST composites with respect to weak and strong ISMs (excluding aborted ENSO years) in the simulation suggest that this out-of-phase relationship between the ISM and WNPSM is largely controlled by the anomalous SST gradient between the North Arabian Sea and the South China Sea during boreal spring (Fig. 12). A weak ISM is preceded by cold SST anomalies in the Arabian Sea and warm SST anomalies in the South China Sea, favoring enhanced precipitation in the western North Pacific and suppressed precipitation over the Indian subcontinent (Figs. 10.a, c). The opposite relationship is observed for strong ISM years in the simulation. Similar SST composites have been presented by Terray et al. (2003, their figures 4 and 5) from the observations. Their results show that weak (strong) ISMs are preceded by significant negative (positive) SST anomalies in the southeastern subtropical Indian Ocean during boreal winter in the observations. Thus, the results obtained from the SINTEX simulation are strikingly different (Fig. 12). Furthermore, Ju and Slingo (1995) propose a mechanism by which the phase of ENSO influences the ISM via anomalous heating over the western North Pacific in the preceding spring. Surprisingly, the SINTEX model also suggests an opposite mechanism, with a competition between heating patterns in the Arabian Sea and the western North Pacific, which is not seen in the observations.

Another intriguing feature is the warm SST anomalies observed in the central and eastern Pacific during winter and spring before weak ISMs in the simulation (Figs. 12.a, c). This last aspect of the simulation seems to play a key role in the lead-lag relationships between ISMs and Niño34 SSTs in the SINTEX model (Figs. 9.b, c). A tedious investigation shows that this behaviour is linked to the fact that years following El Niño years also have a weakened ISM in the simulation (but not in the observations). This is illustrated with the February-March and April-May SST composites with respect to weak ISMs after exclusion of aborted and regular El Niño years in the simulation (Fig. 13). Significant warm SST anomalies are seen in the central and eastern Pacific during winter and spring before weak ISMs, even after the exclusion of all El Niño years in the simulation. Warm SST anomalies are also observed in the western North Pacific in April-May just before the onset of the weak ISMs, as in Fig. 12. This strange behaviour is related to the systematic persistence of El Niño conditions in the central and eastern Pacific until the early summer of years following the events, and with the associated warm SST anomalies in the western North Pacific before ISM onset in the simulation (Fig. 13). Fig. 9.d shows the lead-lag correlation analysis between ISM rainfall and Niño34 SSTs without aborted ENSO years and years following regular El Niño years in the simulation. By excluding the years following regular El Niño events and the aborted ENSO years, the coupled model now captures many aspects of the observed ISM-ENSO relationship, even though the magnitude of the correlations is still less than in the observations (Fig. 9.a). This confirms that El Niño events may affect the ISM of the following year by inducing warm SST anomalies in the western North Pacific, which favor active precipitation anomalies in this area and are accompanied by suppressed precipitation anomalies over the Indian subcontinent during boreal summer in the simulation. This fact contributes significantly to the simulated lead-lag relationship between ISM rainfall and Niño34 SSTs (Figs. 9.b, c, d). This problematic ISM-WNPSM-ENSO relationship may be traced back to SST or physical parameterization errors (in particular in the convection scheme) in the coupled GCM, since there is a close correspondence between precipitation, wind and SST anomalies in the SINTEX simulation.

To clearly illustrate the weaker-than-observed association between the Pacific trade winds and ISMs which results from these problems in the simulation, Figure 14 shows the lead-lag correlations between the ISM IOVS index and monthly time series of the zonal 850 hPa wind over the EQPAC area in observations and the simulation. The observed lag-correlations show that ISM variability defined in terms of the dynamical IOVS index is significantly associated with the strength of the low-level easterlies over the equatorial Pacific particularly during the ISM, but also afterwards, during boreal fall and winter. On the contrary, the coupled model fails to capture this link, with the lagged correlation between the two wind indices near zero during and after the ISM. Seasonal (June-September) correlations between various surface and upper-level wind indices associated with both the ISM and ENSO have been computed in order to examine in more detail the dynamic of the monsoon-ENSO relationships during northern summer (Table 6). During the ISM, none of the correlations between the 200 hPa zonal wind anomalies over the central Pacific and the Indian Ocean wind indices are significant in the NCEP reanalysis. On the other hand, the 850 hPa zonal wind anomalies over the central Pacific are significantly correlated with the 200 hPa zonal wind anomalies over the equatorial Indian Ocean and EIMR region. These correlations are even stronger than the one between the lower and upper-level zonal flows over the central Pacific. The 200 hPa zonal flow over the equatorial and North Indian Ocean is clearly associated with the upper branch of the reverse Hadley cell which characterizes the monsoon (section 3). Thus, these statistical relationships suggest a possible physical mechanism linking ISM variability and the strength of the 850 hPa easterlies over the equatorial Pacific. Both the Tibetan high and the tropical easterly jet in the upper troposphere are considerably weakened during weak ISMs in response to decreased rainfall and latent heat release over the Indian monsoon trough (Kanamitsu and Krishnamurti, 1978; Terray et al., 2003). All of these imply that significant westerly wind anomalies will be observed in the upper atmosphere over the equatorial and north Indian Ocean during weak ISMs (Table 1). These upper-level wind anomalies may then contribute to the filling of the western center of the SO, as indicated by the downward pressure vertical velocity anomalies observed over the maritime continent during weak ISMs (Figs. 10.a, c). This, in turn, would reduce the horizontal pressure gradient across the equatorial Pacific (irrespective of local SST anomalies in this area). The reduced pressure gradient would finally result in a weakening of the trade winds over the equatorial Pacific, as observed (Figs. 10.a, c). A similar argument may be suggested to explain the influence of ENSO on the ISM as depicted in Fig. 8. Moreover, this double interaction may explain the strength of the correlation between the surface zonal wind over the Pacific and the upper-level zonal wind over the Indian Ocean. These various relationships are not well simulated by the SINTEX model (Table 7). In particular, the correlation between the upper-level easterlies over the Indian Ocean and the surface easterlies over the central Pacific is lower than observed, though still significant. More importantly, this correlation is much lower than the one between the 850 and 200 hPa zonal wind over the equatorial Pacific. This corroborates the fact that the Pacific Walker circulation is not significantly affected by ISM variability in the simulation. In turn, this may contribute to the lower-than-observed variability of ENSO indices in the simulation.

The contrasted behaviour seen between the observations and the coupled GCM in the ISM-WNPSM-ENSO relationship suggests that better simulation of the interannual variability in the Indo-Pacific areas with a coupled GCM is strongly dependent upon how well the model captures the annual cycle in these areas, since the coupled model is not able to simulate the western North Pacific annual cycle as demonstrated in Section 3.

5. Conclusions and discussion

In this study, we examined the ability of a state-of-the-art coupled GCM to simulate the observed ENSO-monsoon relationships.

The SINTEX model is able to realistically portray important features of the ISM circulation and rainfall climatology over Indian areas, even though the reversed Hadley cell associated with the ISM is weakened in the simulation. As a consequence, the total area-averaged ISM rainfall is underestimated. This may reflect the sensitivity of the simulated precipitation to the smooth orography used in the atmospheric model (T30 truncation), and deficiencies in the convection parameterization scheme. However, the model captures both the spatial and temporal characteristics of ISM variability. In both observations and simulation, ISM rainfall anomalies are significantly associated with fluctuations of the Hadley circulation over the Indian subcontinent, in agreement with the results of Goswami et al. (1999). The quasi-biennial time-scale is found to structure ISM dynamical and rainfall indices in both the observations and the simulation. Overall features of the model ISM climatology and variability in the coupled model are in closer agreement with the observations than in the recent study of Cherchi and Navarra (2003) which used the same atmospheric model (ECHAM-4 at T30 resolution), but forced with observed SSTs. This stresses the coupled nature of the monsoon system. These conclusions are broadly consistent with the results of the coupled model studies of Meehl and Arblaster (1998), Kitoh et al. (1999) and Fu et al. (2002).

The coupled model is less successful in simulating the annual cycle in the tropical Pacific. The Pacific warm pool is eroded, and the model tends to produce a too-zonal and pronounced southern ITCZ year-round. The seasonal cycle of SST in the eastern Pacific is also reduced and the semiannual cycle is too-present in the equatorial central Pacific. These systematic errors are typical of several global coupled models without flux adjustments, such as those reported by Latif et al. (2002), Davey et al. (2002) and AchutaRao and Sperber (2002). During northern summer, the main bias of the SINTEX simulation is associated with an eastward displacement of the western North Pacific ITCZ near the dateline, and associated underestimation of rainfall off the Philippines. The observed spatial pattern of summer rainfall over the western Pacific is very difficult to simulate (Kang et al., 2002). The ECHAM-4 model used in our coupled simulation has the same problem when forced with observed SSTs (Cherchi and Navarra, 2002). Kang et al. (2002) suggested that the performance of atmospheric GCMs in this area could be again related to the convection scheme and other physical parameterizations used in atmospheric models. In the SINTEX model, this systematic error is also associated with the westward extension of the eastern Pacific cold tongue into the western Pacific, and the anomalous strength of the North Pacific subtropical high during northern summer. Interestingly, our analysis suggests that the various errors noted in the tropical Pacific are intimately related through the organization of two mislocated and seasonally-varying atmospheric cells in the simulation. These errors particularly affect the upper-level wind field over the equatorial Pacific Ocean, and have a profound impact on the annual cycle of the Pacific Walker circulation. A very strong semiannual component with maxima occurring in early northern summer and winter seasons is noted in the simulated 200 hPa westerly wind over the equatorial central Pacific, in total disagreement with observations. During northern summer, the unrealistic and strong upper-level westerlies over the equatorial Pacific are the manifestation of the upper branch of an erroneous cell linking the shifted north western ITCZ and the South Pacific subtropical high.

During the 200 years of the experiment, the model captures roughly 60% of the observed ENSO signal as measured by the Niño34 SST anomalies. It reproduces the annual cycle of variance in the Niño34 SST time series, with maxima during boreal winter and minima in early boreal spring. In other words, most warm events in the simulation are phase-locked with the annual cycle, as observed (Guilyardi et al., 2003). Wavelet decomposition of the model Niño34 time series shows enhanced power in the 2-4 year period, as compared to the 2-8 year range observed during the 1950-2000 interval. Thus, despite problems in the simulation of the mean climate, the coupled model achieves an interannual variability in the tropical Pacific comparable to other current coupled models in Latif et al. (2001), Davey et al. (2002) or AchutaRao et Sperber (2002).

The coupled model reproduces the observed ENSO-related rainfall and circulation anomalies in the Indian area reasonably well. In both the simulation and observations, ISM rainfall anomalies are negatively correlated with Niño34 SST anomalies, and the ISM circulation is weakened during El Niño years. Moreover, there is a reasonable agreement in the observed and simulated atmospheric circulation patterns over the Indian Ocean during El Niño years, even though the coupled model emphasizes the importance of the anomalous anticyclone in the southeast Indian Ocean (Wang et al., 2003) due to a much stronger wind-thermocline-SST feedback off the west coast of Sumatra during boreal summer (Fischer et al., 2003). This aspect of the simulation is also linked to the westward extension of the Pacific regime into the eastern Indian Ocean, which induces a shallower thermocline in the eastern Indian Ocean.

However, the model fails to reproduce the lead-lag relationship between Niño34 SSTs and the ISM. In the observations, weak ISMs are preceded by a transition in boreal spring from a La Niña to an El Niño state in the Pacific. On the other hand, the coupled model shows significant negative correlations prior to the ISM, decreasing during fall and winter after the ISM. Moreover, the correlations are weaker than in the observations. A number of different aspects of the model simulation play a role in this weak ISM-ENSO relationship at the interannual time scale. First, the coupled model also exhibits aborted ENSO events, where the warming peaks in late spring and quickly fades away (Guilyardi et al., 2003). These aborted ENSO events have a significant relationship with the ISM and contaminate the ISM-ENSO relationship in the simulation. Another weakness of the coupled model that may contribute to the unrealistic simulation of the lead-lag relationships between the ISM and ENSO is the less-than-adequate simulation of the SO, due to the erroneous eastward extension of the SPCZ. This is symptomatic of the incorrect location of the South Pacific subtropical anticyclone, a key feature for ENSO-related atmospheric variability. A final aspect of the simulation which seems to play a key role in this problem is that years following El Niño events also have a weakened ISM in the simulation, but not in the observations. This is due to the persistence of El Niño conditions in the Pacific and to the related warm SST anomalies appearing in the western North Pacific during spring after El Niño events in the simulation. These warm SST anomalies favor active precipitation anomalies in the western North Pacific, and are accompanied by suppressed precipitation anomalies over the Indian subcontinent during boreal summer. By excluding the years following El Niño events and aborted ENSO years from the statistical analysis, the coupled model captures many aspects of the observed ISM-ENSO relationship.

Thus, the weaker-than-observed association between the ISM and ENSO is mainly due to the unrealistic anomalous atmospheric patterns simulated by the coupled model over the western North Pacific during anomalous ISMs and ENSO events. The amplitude and even the sign of the simulated surface wind anomalies in these areas are not consistent with observed patterns during anomalous ISMs or ENSO years. These errors induce a strong competition between the ISM and WNPSM in the simulation. The correlation between ISM and WNPSM rainfall indices is near-zero and statistically insignificant in the observations, but negative and significant in the simulation. The anomalous SST gradient between the North Arabian Sea and the South China Sea during boreal spring seems to play an important role in this out-of-phase relationship between the ISM and WNPSM. Warmer SSTs in the Arabian Sea and colder SSTs in the South China Sea during spring favor more rainfall over India, but suppress convective activity east of the Philippines. The reverse relationship also holds in the simulation. The incorrect simulation of WNPSM variability may be due to the systematic errors in the Pacific annual cycle and, more precisely, to the extension of the eastern equatorial Pacific cold tongue regime into the warm pool and to the related eastward displacement of the main convective center associated with the WNPSM.

The out-of-phase relationship between the ISM and WNPSM also has a pronounced effect on the 850 hPa wind anomaly pattern simulated over the central Pacific during anomalous ISMs. Lag correlations show that the delayed response of the wind stress over the central Pacific to ISM variability is very small in the simulation. In other words, systematic errors in simulating the seasonal cycle over the tropical Pacific isolate the Pacific Walker circulation from ISM forcing during northern summer. This has the effect of disrupting the close observed association between the wind stress over the equatorial central Pacific and the ISM at the interannual time scale. This systematic error may affect the amplitude of ENSO variability and contribute to explaining why most simulated ENSO indices have lower-than-observed variance in the SINTEX simulation.

During the course of the SINTEX project, the oceanic component ORCA has been coupled with ECHAM-4 at three different resolutions (T30, T42, T106) in long control experiments. Our future work will assess the possible impact of the horizontal resolution of the atmospheric component on reducing the systematic errors analyzed in this study.

Acknowledgments

We would like to thank Sebastien Masson for providing graphical software and for his help. The perceptive comments of A. Navarra and one anonymous reviewer are gratefully acknowledged. The NCAR/NCEP reanalysis data was provided through the NOAA Climate Center (http://www.cdc.noaa.gov). Wavelet software was provided by C. Torrence and G. Compo, and is available at URL: http://paos.colorado.edu/research/wavelets/. Computations were performed at the French Institute for Development and Resources in Scientific Computing (IDRIS). This research was supported by the French Programme National d'Etude Du Climat (PNEDC) and SINTEX projects (Environnement Program, Contract n°ENV4-CT98-0714). ASF was supported by a grant from the Swiss Federal Office of Education and Science (BBW/OFES).

REFERENCES

AchutaRao, K., and K.R. Sperber, 2002: Simulation of the El Niño Southern Oscillation: Results from the Coupled Model Intercomparison Project. *Clim. Dyn.*, 19, 191-209.

Ailikun, B., and T. Yasunari, 2001: ENSO and Asian Summer Monsoon : Persistence and Transitivity in the Seasonal March. *J. Meteor. Soc. Japan*, 79, 145-159.

Annamalai, H., J.M. Slingo, K.R. Sperber, and K. Hodges, 1999: The mean evolution and variability of the Asian summer monsoon: Comparison of ECMWF and NCEP/NCAR reanalysis. *Mon. Wea. Rev.*, 127, 1157-1186.

Chen, T.C., and H. Van Loon, 1987: Interannual variation of the tropical easterly jet. *Mon. Wea. Rev.*, 115, 1739-1759.

Cherchi, A., and A. Navarra, 2003: Reproducibility and predictability of the Asian summer monsonn in the ECHAM4-GCM. *Clim. Dyn.*, in press.

Davey, M.K., et al., 2002: STOIC: a study of coupled model climatology and variability in tropical ocean regions. *Clim. Dyn.*, 18, 403-420.

Elliott, W.P., and J.K. Angell, 1987: The relation between Indian monsoon rainfall, the Southern Oscillation, and hemispheric air and sea temperature 1884-1984. *J. Climate Appl. Meteor.*, 26, 943-948.

Fennessy, M.J., and Coauthors, 1994: The simulated Indian monsoon: A GCM sensitivity study. *J. Climate*, 7, 33-43.

Fischer, A.S., P. Terray, E. Guilyardi, S. Gualdi, and P. Delecluse, 2003: Triggers for tropical Indian Ocean variability and links to ENSO in a constrained coupled GCM. In revision for *J. Climate*.

Fu, X., B. Wang, and T. Li, 2002: Impacts of air-sea coupling on the simulation of mean Asian summer monsoon in the ECHAM4 model. *Mon. Wea. Rev.*, 130, 2889-2904.

Gadgil, S., and S. Sajani, 1998: Monsoon precipitation in the AMIP runs. *Clim. Dyn.*, 14, 659-689.

Gill, A.E., 1980: Some simple solutions for heat-induced tropical circulation. *Quart. J. Roy. Meteor. Soc.*, 106, 447-462.

Goswami, B. N., V. Krishnamurty, and H. Annamalai, 1999: A broad-scale circulation index for the interannual variability of the Indian summer monsoon. *Q. J. R. Meteorol. Soc.*, 125, 611-633.

Goswami, B. N., and V. Jayavelu, 2001: On the possible Impact of the Indian Summer Monsoon on the ENSO. *Geophys. Res. Lett.*, 28, 571-574.

Gualdi S, A. Navarra, E. Guilyardi, and P. Delecluse, 2003a : The SINTEX coupled GCM. The tropical Indo-Pacific region. *Annals of Geophys*. 46, 1-26.

Gualdi, S., E. Guilyardi, A. Navarra, S. Masina and P. Delecluse, 2003b: The interannual variability in the tropical Indian Ocean as simulated by a coupled GCM. *Clim. Dyn*., 20, 567-582.

Guilyardi E, P. Delecluse, S. Gualdi, A. Navarra, 2003 : Mechanisms for ENSO phase change in a coupled GCM. *J. Clim*., 16, 1141-1158.

Hastenrath, S., 2000 : Zonal circulations over the equatorial Indian Ocean. *J. Clim*., 13, 2746-2756.

Joseph , P.V., J.K. Eischeid and R.J. Pyle, 1999: Interannual variability of the onset of the Indian summer monsoon and its association with atmospheric features, El Nino and sea surface temperature anomalies; J. Climate, 7, 81-105.

Ju J., and J. Slingo, 1995: The Asian summer monsoon and ENSO. *Q. J. R. Meteorol. Soc*., 121, 1133-1168.

Kalnay, E., and Coauthors, 1996: The NCEP/NCAR 40-year reanalysis project. *Bull. Amer. Meteor. Soc*., 77, 437-471.

Kanamitsu, M., and T.N. Krishnamurti, 1978: Northern summer tropical circulations during drought and normal rainfall months. *Mon. Wea. Rev*., 106, 331-347.

Kang, I.-S., and al., 2002: Intercomparison of the climatological variations of Asian summer monsoon precipitation simulated by 10 GCMs. *Clim. Dyn*., 19, 383-395.

Kawamura, R., 1998: A possible mechanism of the Asian summer monsoon-ENSO coupling. *J. Meteor. Soc. Japan*, 76, 1009-1027.

Kim, K.M., and K.M. Lau, 2001: Dynamics of monsoon-induced biennial variability in ENSO. *Geophys. Res. Lett*., 28, 315-318.

Kirtman, B. P., and J. Shukla, 2000: Influence of the Indian summer monsoon on ENSO. *Q. J. R. Meteorol. Soc*., 126, 213-239.

Kirtman, B. P., and S.E. Zebiak, 1997: ENSO simulation and prediction with a hybrid coupled model. *Mon. Wea. Rev*., 125, 2620-2641.

Kitoh, A., S. Yukimoto and A. Noda, 1999: ENSO-Monsoon Relationship in the MRI Coupled GCM. *J. Meteorol. Soc. Japan*, 77, 1221-1245.

Krishnamurti, T.N. and H.N. Bhalme, 1976: Oscillations of a monsoon system. Part I. Observational aspects. *J. Atmos. Sci*., **33**, 1937-1954.

Lal, M., U. Cubasch, J. Perlwitz and J. Waszkewitz, 1997: Simulation of the Indian monsoon climatology in the ECHAM3 climate model: sensitivity to horizontal resolution. *Int. J. Climatol*., 17, 847-858.

Latif, M., et al., 2001: ENSIP: the El Niño simulation intercomparison project. *Clim. Dyn.*, 18, 255-276.

Lau, N.C., and M.J. Nath, 2000: Impact of ENSO on the variability of the Asian-Australian monsoons as simulated in GCM experiments. *J. Climate*, 13, 4287-4309.

Levitus, S., 1982: Climatological Atlas of the world ocean. NOAA professional paper No. 13, 173 pp.

Li, T., B. Wang, C.P. Chang and Y.S. Zhang, 2003: A theory for the Indian Ocean Dipole-Zonal Mode. J. Atmos. Sci., 60, 2119-2135.

Madec G, P. Delecluse, M. Imbard, and C. Levy, 1998 : OPA version 8.1 ocean general circulation model reference manual. Technical Report, LODYC/IPSL, Note 11, Paris, France, pp 91.

Mechoso, M.R., and Coauthors, 1995: The seasonal cycle over the tropical Pacific in coupled ocean-atmosphere general circulation models. *Mon. Wea. Rev.*, 123, 2825-2838.

Meehl, G. A., 1987: The annual cycle and interannual variability in the tropical Indian and Pacific Ocean regions. *Mon. Wea. Rev.*, 115, 27-50.

Meehl, G. A., 1997: The South Asian monsoon and the tropospheric biennial oscillation. *J. Climate*, 10, 1921-1943.

Meehl, G. A., and J. M. Arblaster, 1998: The Asian-Australian Monsoon and El Niño-Southern Oscillation in the NCAR Climate System Model. *J. Climate*, 11, 1356-1385.

Meehl, G.A., P.R. Gent, J.M. Arblaster, B.L. Otto-Bliesner, E.C. Brady and A. Craig, 2001: Factors that affect the amplitude of El Niño in global coupled climate models. *Clim. Dyn.*, 17, 515-526.

Meehl, G.A., and J. Arblaster, 2002a: The tropospheric biennial oscillation and the Asian-Australian monsoon rainfall. *J. Climate*, 15, 722-744.

Meehl, G.A., and J. Arblaster, 2002b: Indian monsoon GCM sensitivity experiments testing tropospheric biennial oscillation transition conditions. *J. Climate*, 15, 923-944.

Ogasawara, N., A. Kitoh, T. Yasunari, and A. Noda, 1999: Tropospheric biennial oscillation of the ENSO-monsoon system in the MRI coupled GCM. *J. Meteorol. Soc. Japan*, 77, 1247-1270.

Parthasarathy, B., A.A. Munot, and D.R. Kothawale, 1995: Monthly and seasonal rainfall series for all India, homogeneous regions and meteorological subdivisions: 1871-1994. Indian Institute of Tropical Meteorology Research Rep. RR-065.

Rajendran, K., A. Kitoh, and S. Yukimoto, 2004: South and east Asian summer monsoon climaye and variation in the MRI coupled model (MRI-CGCM2). *J. Climate*, 17, 763-782.

Rasmusson, E.M., and T.H. Carpenter, 1983: The relationship between eastern equatorial Pacific sea surface temperatures and rainfall over India and Sri Lanka, *Mon. Weather Rev.*, 111, 517-528.

Roeckner E, and Coauthors, 1996 : The atmospheric general circulation model Echam-4: model description and simulation of present-day climate. Max-Planck-Institut für Meteorologie, Rep 218, Hamburg, Germany, pp 90.

Slingo, J.M., M. Blackburn, A. Betts, R. Brugge, K. Hodges, B. Hoskins, M. Miller, L. Steenman-Clark and J. Thuburn, 1994: Mean climate and transience in the tropics of the UGAMP GCM: Sensitivity to convective parametrization. *Quart. J. Roy. Meteor. Soc.*, 120, 881-922.

Slingo, J.M., and H. Annamalai, 2000: 1997: The El Niño of the century and the Response of the Indian Summer Monsoon. *Mon. Wea. Rev.*, 128, 1778-1797.

Smith, T.M., R.W. Reynolds, R.E. Livezey, and D.C. Stokes, 1996: Reconstruction of historical sea surface temperatures using empirical orthogonal functions. *J. Climate*, 9, 1403-1420.

Soman, M.K., and J.M. Slingo, 1997: Sensitivity of the Asian summer monsoon to aspects of the sea surface temperature anomalies in the tropical Pacific Ocean. *Quart. J. Roy. Meteor. Soc.*, 123, 309-336.

Sperber, K.R., and T.N. Palmer, 1996: Interannual tropical rainfall variability in general circulation model simulations associated with the Atmospheric Model Intercomparison Project. *J. Clim.*, 9, 2727-2750.

Terray, P., P. Delecluse, S. Labattu and L. Terray, 2003: Sea Surface Temperature Associations with the Late Indian Summer Monsoon. *Clim. Dyn.*, 21, 593-618.

Torrence C., and P. Compo, 1998: A practical guide to Wavelet Analysis. *Bull. Amer. Meteor. Soc.*, 79, 61-78.

Torrence C., and P.J. Webster, 1998: The annual cycle of persistence in the El Niño/Southern Oscillation. *Q. J. R. Meteorol. Soc.*, 124, 1985-2004.

Trenberth, K.E., 1997: The definition of El Niño. *Bull. Amer. Meteor. Soc.*, 78, 2771-2777.

Trenberth, K.E., and J.M. Caron, 2000: The Southern Oscillation revisited: Sea level pressures, surface temperatures and precipitation. *J. Climate*, 13, 4358-4365.

Valcke S, L. Terray, and A. Piacentini, 2000 : The OASIS coupler user guide version 2.4. Technical Report, TR/CMGC/00-10, CERFACS, Toulouse, France, pp 85

Walker, G.T., 1923: Correlation in seasonal variations of weather VIII. *Mem. Indian Meteor. Dept.*, 24, 75-131.

Wang, B., and Z. Fan, 1999: Choice of South Asian summer monsoon indices. *Bull. Amer. Meteor. Soc.*, 80, 629-638.

Wang, B., R. Wu and R. Lukas, 1999: Roles of the western North Pacific wind variation in thermocline adjustment and ENSO phase transition. *J. Meteor. Soc. Japan*, 77, 1-16.

Wang, B., R. Wu, and K.-M. Lau, 2001: Interannual Variability of the Asian Summer Monsoon: Contrasts between the Indian and the Western North Pacific–East Asian Monsoons. *J. Climate*, 14, 4073-4090.

Wang B., R. Wu and T. Li, 2003: Atmosphere-Warm Ocean Interaction and its Impacts on Asian-Australian Monsoon Variation. *J. Climate*, 16, 1195-1211.

Webster P. J., and S. Yang, 1992: Monsoon and ENSO: Selectively interactive systems. *Q. J. R. Meteorol. Soc.*, 118, 877-926.

Webster, P.J., V.O. Magana, T.N. Palmer, J. Shukla, R.A. Tomas, M. Yanai, and T. Yasunari, 1998: Monsoons: Processes, predictability and the prospects for prediction. *J. Geophys. Res.* , 103 (C7), 14 451-14 510.

Xie P., and P.A. Arkin, 1997 : Global precipitation: A 17-year monthly analysis based on gauge observations, satellite estimates and numerical model outputs. *Bull. Amer. Meteor. Soc.*, 78, 2539-2558.

Yasunari, T., 1990: Impact of Indian monsoon on the coupled atmosphere/ocean systems in the tropical Pacific. *Meteor. Atmos. Phys.*, 44, 29-41.

Young, J.A., 1987: Physics of monsoons: The current view. Monsoons. J.S. Fein and P.L. Stephens Eds. John Wiley and Sons, 211-243.

FIGURE CAPTIONS

Figure 1: 850 hPa wind and 500 hPa vertical pressure velocity (omega) climatology. a) and c), as derived from the NCEP reanalysis for July and January, respectively. b) and d), as derived from the SINTEX model for July and January.

Figure 2: Same as Figure 1, but for the 200 hPa wind and SLP climatology.

Figure 3: Same as Figure 1, but for the rainfall climatology.

Figure 4: Climatological seasonal cycle of precipitation (mm/day) averaged over the IMR area for the observations and the SINTEX model. The observed IMR is from Parthasarathy et al. (1995). In the simulation, IMR is defined as the area-averaged precipitation over all land grid-points in the domain 75°E-85°E, 10°N-25°N.

Figure 5: Climatological seasonal cycle of 850 and 200 hPa wind components area-averaged over the EIMR (70°E-110°E, 5°N-30°N) and EQIO (60°E-90°E, 2°5 S-2°5 N) areas for the NCEP reanalysis and the SINTEX model. a) 850 hPa zonal wind over the EIMR area. b) 200 hPa zonal wind over the EIMR area. c) 850 hPa meridional wind over the EIMR area. d) 200 hPa meridional wind over the EIMR area. e) 850 hPa zonal wind over the EQIO area. f) 200 hPa zonal wind over the EQIO area.

Figure 6: Climatological seasonal cycle of the SST along the equator (averaged between 5°S and 5°N) in the Indian and Pacific Oceans. a) As derived from the Reynolds dataset. b) As derived from the SINTEX model. The vertical axis represents time, the horizontal axis longitude.

Figure 7: Climatological seasonal cycle of 850 and 200 hPa zonal wind area-averaged over the EQPAC area (160°W-130°W, 2°5 S-2°5 N) for the NCEP reanalysis and the SINTEX model. a) 850 hPa zonal wind over the EQPAC area. b) 200 hPa zonal wind over the EQPAC area.

Figure 8: Composite analysis of 850 hPa wind (m/s) and 500 hPa vertical pressure velocity (Pa/s) fields with respect to El Niño years from the NCEP reanalysis and the

SINTEX simulation. The El Niño years are defined with the help of Niño34 SST anomaly. See text for more details. May, June, July, August and September composites during the El Niño years are presented. Only the 90% statistically significant 850 hPa wind anomalies are shown. a), c), e), g) and i) from the NCEP reanalysis. b), d), f), h) and j) from the SINTEX model.

Figure 9: Lead/lag correlations between IMR time series and the monthly Niño34 SST anomaly. a) For the observations (1871-1998 period). b) For the SINTEX simulation (200 years). c) For the SINTEX simulation, but without aborted ENSO years. d) For the SINTEX simulation, but without aborted ENSO years and years following regular El Niño years. Also shown below or above the correlation bars are critical probability associated with each correlation coefficient. These probabilities have been computed with a classical two tail t-test since all the correlations are based on yearly sampled series showing insignificant lag-1 autocorrelations.

Figure 10: Composite analysis of 850 hPa wind (m/s), and 500 hPa vertical pressure velocity (Pa/s) fields with respect to weak ISM years from the NCEP reanalysis (1948-1998 period) and the SINTEX simulation. The weak ISM years are defined with the help of the IMR index. The weak ISMs which are also aborted El Niño years have been excluded from the composites in the simulation. See text for more details. Only the 90% statistically significant 850 wind anomalies are shown. a) and c) 850 hPa wind and 500 hPa omega composites for June-July and August-September from the NCEP reanalysis, respectively. b) and d) same as a) and c), but for the SINTEX simulation.

Figure 11: Same as Figure 10, but for the strong ISMs.

Figure 12: a) and c) Composite analysis of February-March and April-May SST fields with respect to weak ISMs in the SINTEX simulation. b) and d) probability maps showing critical probabilities associated with the composite maps in a) and b), respectively. Only the 10, 1, 0.1% confidence levels are plotted. e), f), g) and h) same as a), b), c) and d), but for strong ISMs in the SINTEX simulation. The anomalous ISMs which are also aborted ENSO years have been excluded from the composites. See text for more details.

Figure 13: a) and c) Composite analysis of February-March and April-May SST fields with respect to weak ISMs which are not regular or aborted El Niño years in the SINTEX simulation. b) and d) probability maps showing critical probabilities associated with the composite maps in a) and b), respectively. Only the 10, 1, 0.1% confidence levels are plotted. See text for more details.

Figure 14: Same as in Figures 9.a,b, but for the summer (June-September) IOVS index and the EQPAC monthly 850 hPa zonal wind time series from the NCEP reanalysis (1948-1998 period) and the SINTEX simulation (200 years).

TABLE CAPTIONS

Table 1. Cross-correlations between different monsoon rainfall and dynamical indices computed from the observations. WNPSM rainfall indice is computed from the CMAP dataset during 1979-1998. Statistical significance at the 1%, 0.1% and 0.01% are shown by one, two, three asterisks, respectively. Statistical significance has been assessed by a classical two tail t-test. See the text for the definition of the indices.

Table 2. Same as Table 1, but for monsoon rainfall and dynamical indices computed from the SINTEX simulation.

Table 3. Standard deviations (°C) of Niño12, Niño3, Niño34 and Niño4 monthly time series in the simulation and observations. The standard deviations (STD) are computed during the 1950-2000 period for the observations and during the 200 years of the integration for the model experiment.

Table 4. Composite anomalies and statistics of standardized ISM rainfall and dynamical indices for 13 El Niño years extracted from the observations during the period 1948-1998. Anomalies significant (mean) at the 1%, 0.1% and 0.01% are shown by one, two, three asterisks, respectively. Min and Max refer to the minimum and maximum standardized anomalies observed among the 13 El Niño years.

Table 5. Same as Table 4, but for standardized monsoon (both ISM and WNPSM) rainfall and dynamical indices for 37 regular and 17 aborted El Niño years extracted from the SINTEX simulation. The regular and aborted El Niño years are defined with the help of SST Niño34 time series. See text for more details.

Table 6. Seasonal (June-September) cross-correlations between various surface and upper-level atmospheric wind indices in the Indo-Pacific area. All the time series are computed from the NCEP reanalysis during 1948-1998. Statistical significance at the 1%, 0.1% and 0.01% are shown by one, two, three asterisks, respectively. Statistical significance has been assessed by a classical two tail t-test. See the text for the definition of the indices.

Table 7. Same as Table 6, but for surface and upper-level atmospheric wind indices computed from the SINTEX simulation.

Tables

Table 1

Variable	WNPSM (1979-1998)	IMR (1979-1998)	IMR (1948-1998)
IOVS	-0.19	0.40	0.57***
EIMR(v850)	-0.35	0.22	0.24
EIMR(v200)	-0.06	-0.36	-0.50***
IOUS	0.72***	0.09	0.36*
EIMR(u850)	0.54*	-0.06	0.13
EIMR(u200)	-0.60**	-0.22	-0.48**
IOW	0.43	-0.18	0.04
EQIO(u850)	0.22	-0.55*	-0.29
EQIO(u200)	-0.42	-0.28	-0.36*
WNPSM	1	-0.06	

Table 2

Variable	WNPSM	IMR
IOVS	-0.38***	0.68***
EIMR(v850)	-0.40***	0.63***
EIMR(v200)	0.28***	-0.59***
IOUS	0.26**	0.17
EIMR(u850)	0.48***	-0.22*
EIMR(u200)	0.05	-0.49***
IOW	-0.31***	0.37***
EQIO(u850)	-0.28***	0.13
EQIO(u200)	0.24**	-0.48***
WNPSM	1	-0.37***

Table 3

	STD (observation)	STD (simulation)
Niño12	1.15	0.50
Niño3	0.93	0.48
Niño34	0.88	0.43
Niño4	0.63	0.34

Table 4

Variable	Mean	Min	Max
IMR	-0.81**	-2.29	0.88
IOVS	-0.38	-2.58	1.22
EIMR(v200)	0.40	-1.60	2.74
EIMR(v850)	-0.11	-1.93	1.06
IOUS	-0.34	-3.18	1.02
EIMR(u200)	0.74*	-0.63	2.62
EIMR(u850)	0.17	-1.34	1.13
IOW	-0.60*	-3.51	1.32
EQIO(u200)	0.68*	-0.69	2.66
EQIO (u850)	-0.20	-2.20	1.22

Table 5

	Regular El Niño			Aborted El Niño		
Variable	Mean	Min	Max	Mean	Min	Max
IMR	-0.41*	-2.44	1.25	-0.72*	-2.12	0.73
WNPSM	0.53**	-1.47	2.70	0.26	-1.55	2.91
IOVS	-0.30	-2.64	1.77	-0.65*	-2.06	0.28
EIMR(v200)	0.21	-2.04	2.58	0.53	-1.13	1.98
EIMR(v850)	-0.33	-2.12	1.10	-0.63*	-2.55	0.34
IOUS	0.09	-1.81	1.71	-0.57	-1.82	0.99
EIMR(u200)	0.27	-1.61	2.55	0.90**	0.12	2.18
EIMR(u850)	0.42*	-1.43	2.72	-0.01	-1.6	1.98
IOW	-0.39*	-2.48	1.74	-0.32	-1.99	1.77
EQIO(u200)	0.29	-1.58	2.45	0.50	-1.72	2.85
EQIO(u850)	-0.35	-2.02	2.05	-0.04	-1.27	1.23

Table 6

Variable	EQPAC(u850)	EQPAC(u200)
EQPAC(u200)	-0.63***	1
EQIO(u200)	0.69***	-0.23
EQIO(u850)	-0.04	0.26
EIMR(u200)	0.67***	-0.35
EIMR(u850)	-0.39*	0.01
EIMR(v200)	-0.04	0.02
EIMR(v850)	-0.66***	0.29

Table 7

Variable	EQPAC(u850)	EQPAC(u200)
EQPAC(u200)	-0.65***	1
EQIO(u200)	0.30***	-0.20*
EQIO(u850)	-0.27***	0.24**
EIMR(u200)	0.36***	-0.24**
EIMR(u850)	0.02	-0.02
EIMR(v200)	0.09	-0.09
EIMR(v850)	-0.15	0.17

Figure 1

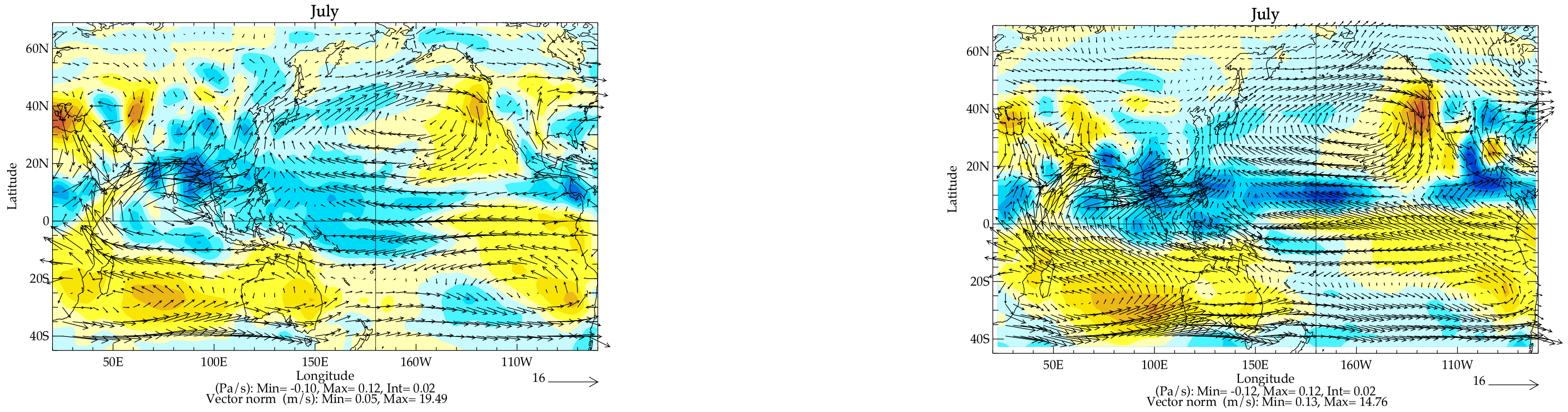
a)

850 hPa Wind and 500 hPa Omega Climatology - NCEP (1950-2000) -

b)

850 hPa Wind and 500 hPa Omega Climatology - SINTEX (1-200) -

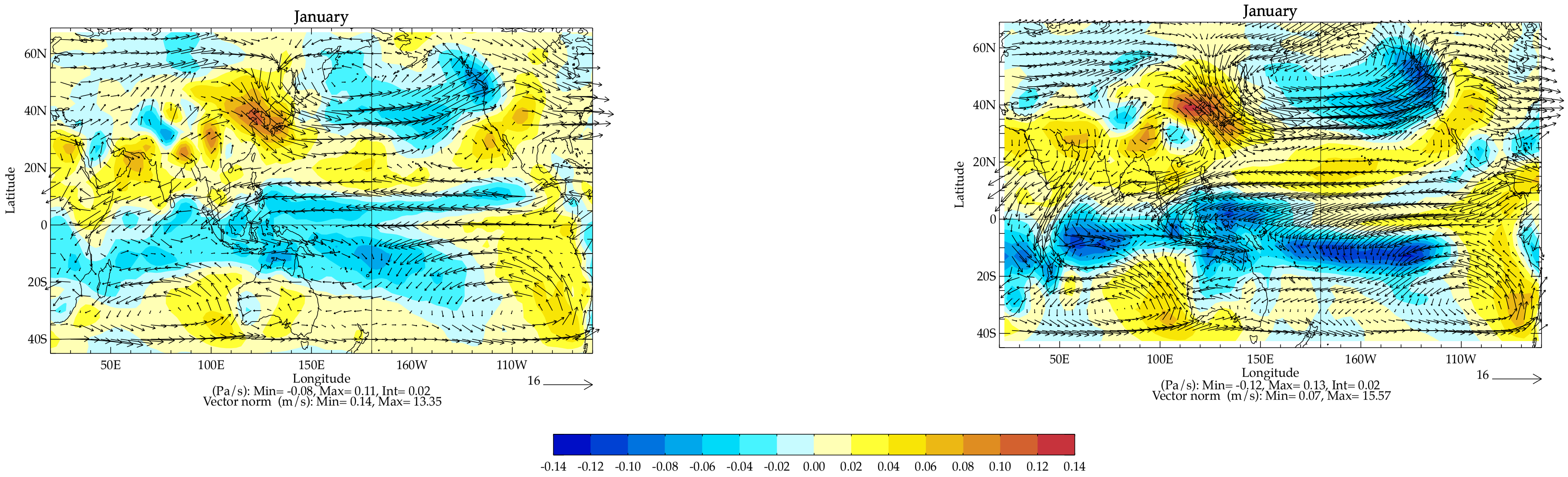
c)

850 hPa Wind and 500 hPa Omega Climatology - NCEP (1950-2000) -

d)

850 hPa Wind and 500 hPa Omega Climatology - SINTEX (1-200) -

Figure 2

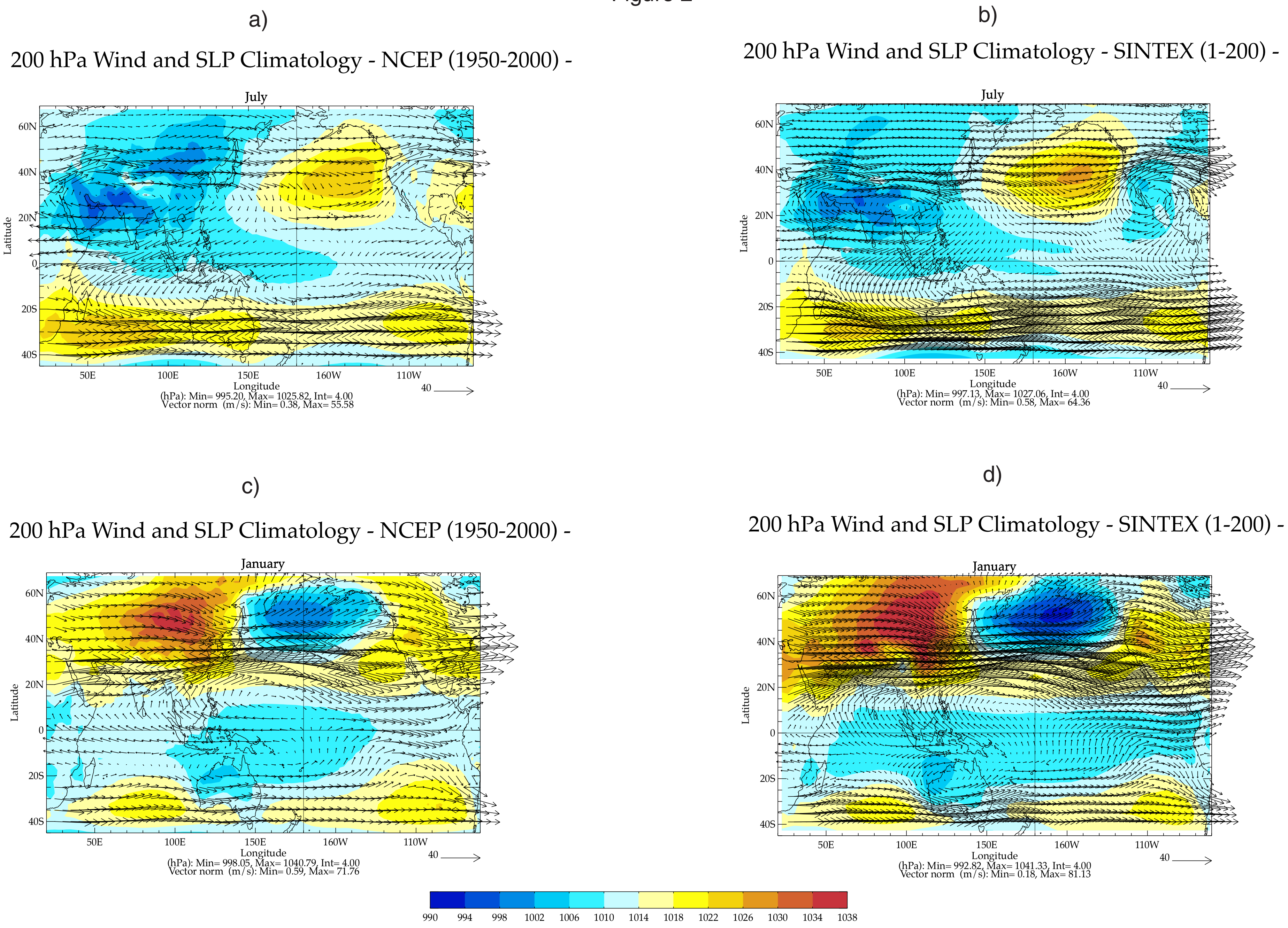
a)
200 hPa Wind and SLP Climatology - NCEP (1950-2000) -
July
60N
40N
20N
0
20S
40S
Latitude
50E
100E
150E
160W
110W
Longitude
(hPa): Min= 995.20, Max= 1025.82, Int= 4.00
Vector norm (m/s): Min= 0.38, Max= 55.58
40
b)
200 hPa Wind and SLP Climatology - SINTEX (1-200) -
July
(hPa): Min= 997.13, Max= 1027.06, Int= 4.00
Vector norm (m/s): Min= 0.58, Max= 64.36
c)
200 hPa Wind and SLP Climatology - NCEP (1950-2000) -
January
(hPa): Min= 998.05, Max= 1040.79, Int= 4.00
Vector norm (m/s): Min= 0.59, Max= 71.76
d)
200 hPa Wind and SLP Climatology - SINTEX (1-200) -
January
(hPa): Min= 992.82, Max= 1041.33, Int= 4.00
Vector norm (m/s): Min= 0.18, Max= 81.13
990
994
998
1002
1006
1010
1014
1018
1022
1026
1030
1034
1038

Figure 3

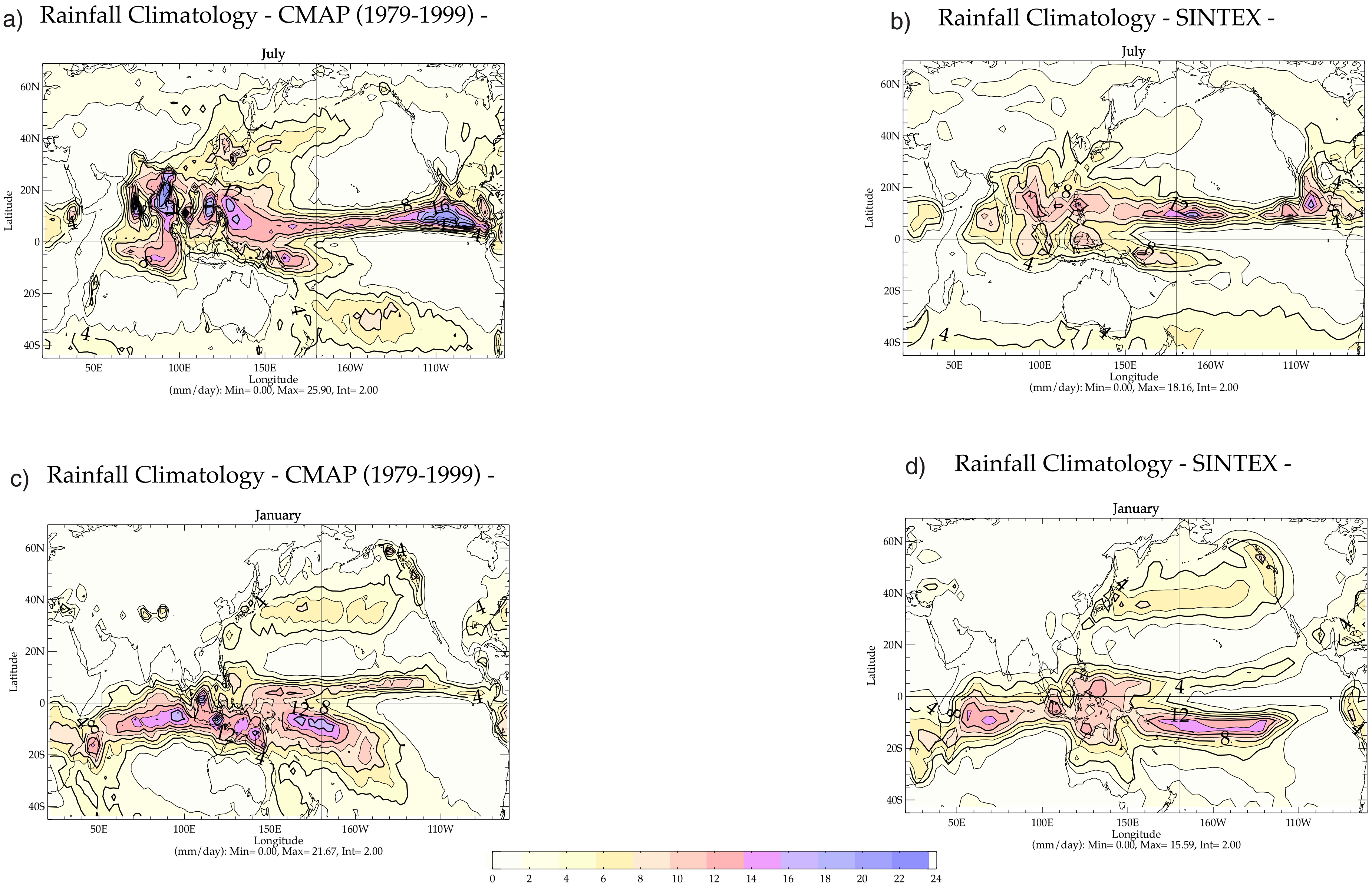

a) Rainfall Climatology - CMAP (1979-1999) -

b) Rainfall Climatology - SINTEX -

c) Rainfall Climatology - CMAP (1979-1999) -

d) Rainfall Climatology - SINTEX -

Figure 4

Climatological seasonal cycle of precipitation (mm/day) averaged over the IMR area

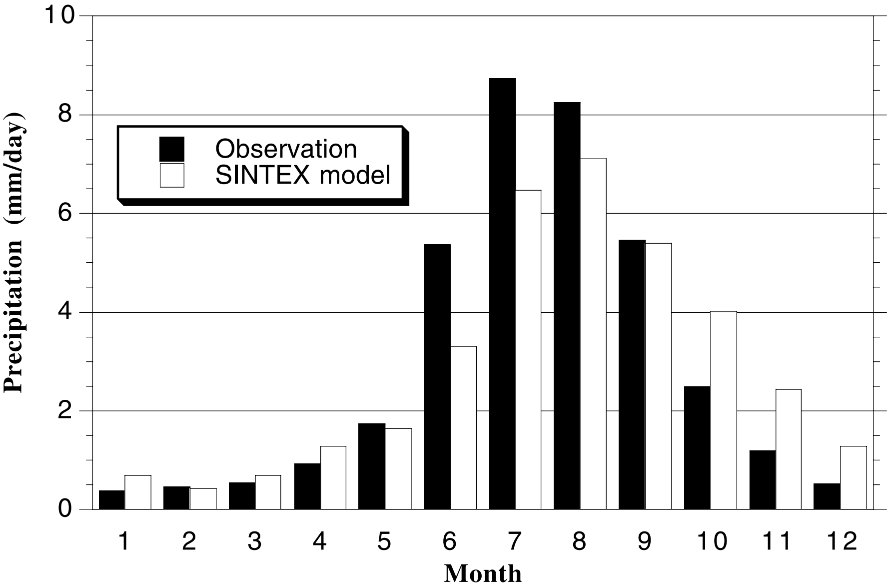

Figure 5

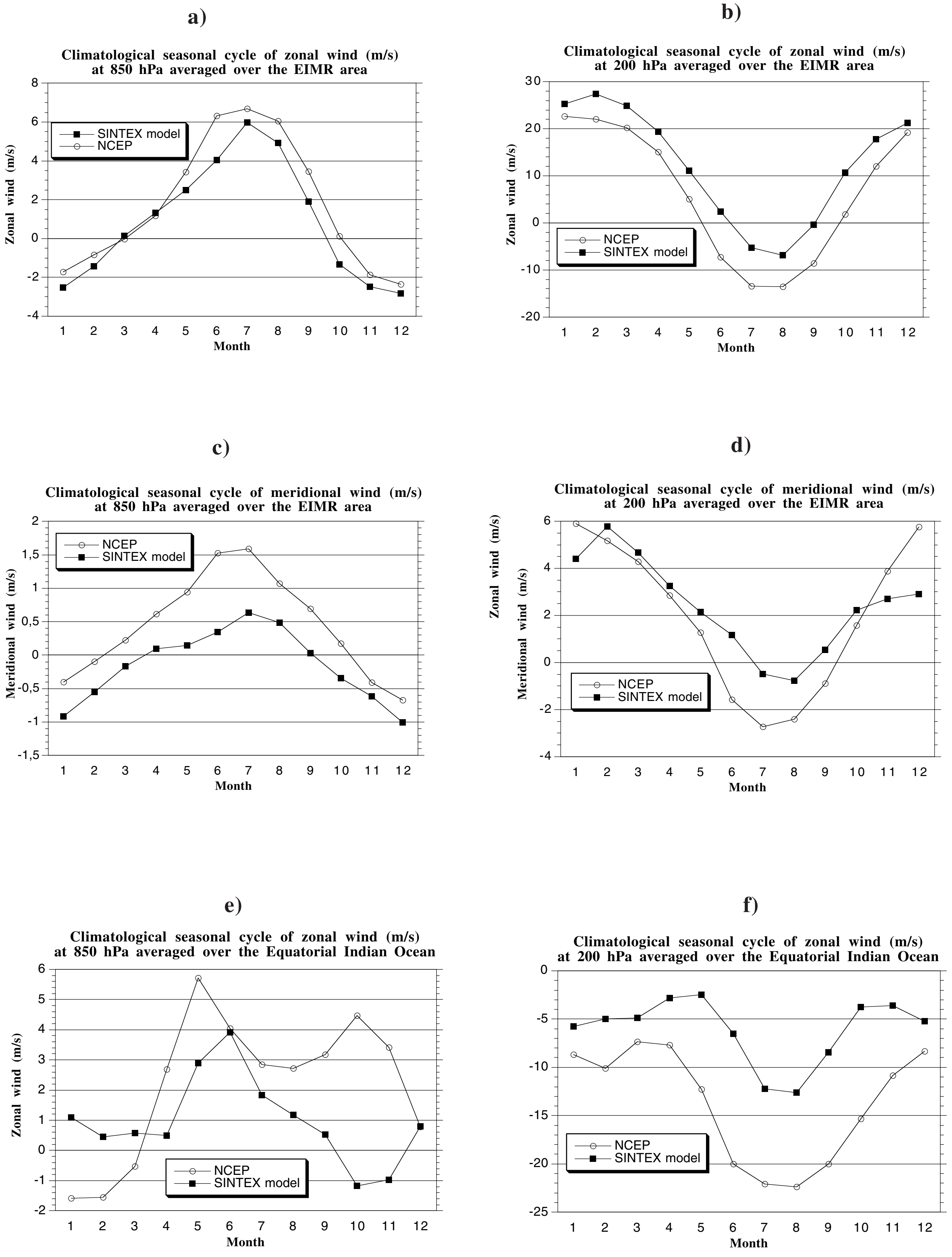

a) Climatological seasonal cycle of zonal wind (m/s) at 850 hPa averaged over the EIMR area

b) Climatological seasonal cycle of zonal wind (m/s) at 200 hPa averaged over the EIMR area

c) Climatological seasonal cycle of meridional wind (m/s) at 850 hPa averaged over the EIMR area

d) Climatological seasonal cycle of meridional wind (m/s) at 200 hPa averaged over the EIMR area

e) Climatological seasonal cycle of zonal wind (m/s) at 850 hPa averaged over the Equatorial Indian Ocean

f) Climatological seasonal cycle of zonal wind (m/s) at 200 hPa averaged over the Equatorial Indian Ocean

Figure 6

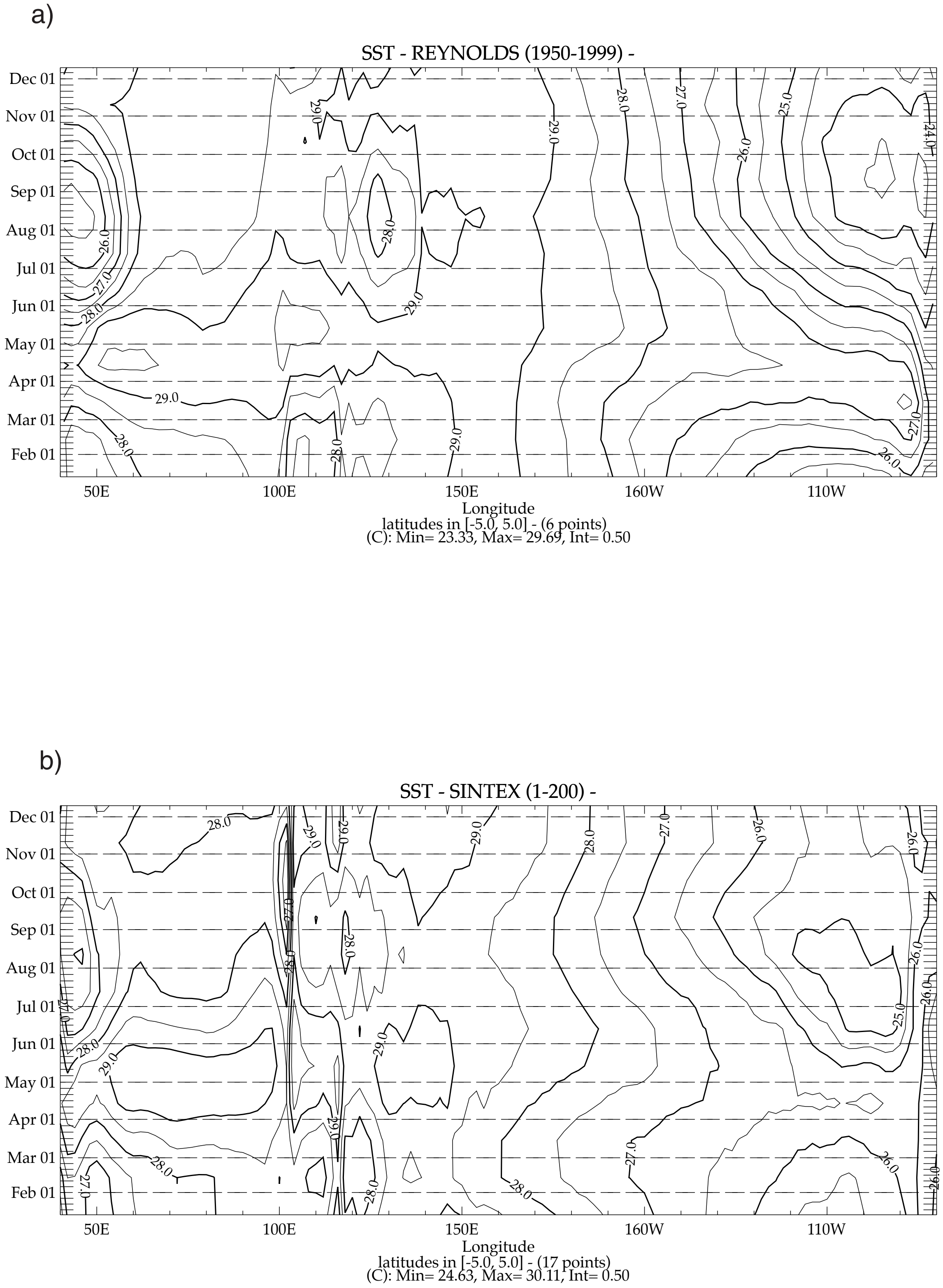
a)
SST - REYNOLDS (1950-1999) -
Dec 01
Nov 01
Oct 01
Sep 01
Aug 01
Jul 01
Jun 01
May 01
Apr 01
Mar 01
Feb 01
29.0
28.0
27.0
26.0
25.0
24.0
50E
100E
150E
160W
110W
Longitude
latitudes in [-5.0, 5.0] - (6 points)
(C): Min= 23.33, Max= 29.69, Int= 0.50
b)
SST - SINTEX (1-200) -
Dec 01
Nov 01
Oct 01
Sep 01
Aug 01
Jul 01
Jun 01
May 01
Apr 01
Mar 01
Feb 01
29.0
28.0
27.0
26.0
25.0
50E
100E
150E
160W
110W
Longitude
latitudes in [-5.0, 5.0] - (17 points)
(C): Min= 24.63, Max= 30.11, Int= 0.50

Figure 7

a) Climatological seasonal cycle of zonal wind (m/s) at 850 hPa averaged over the Equatorial Pacific

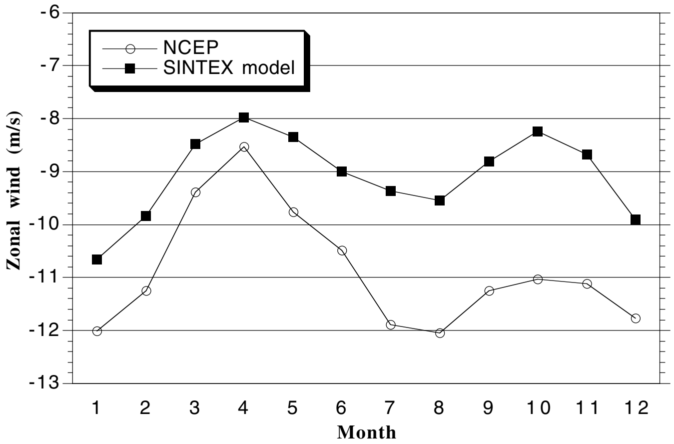

b) Climatological seasonal cycle of zonal wind (m/s) at 200 hPa averaged over the Equatorial Pacific

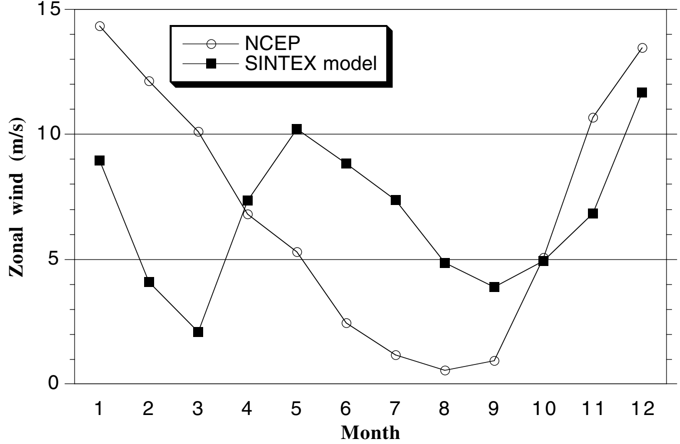

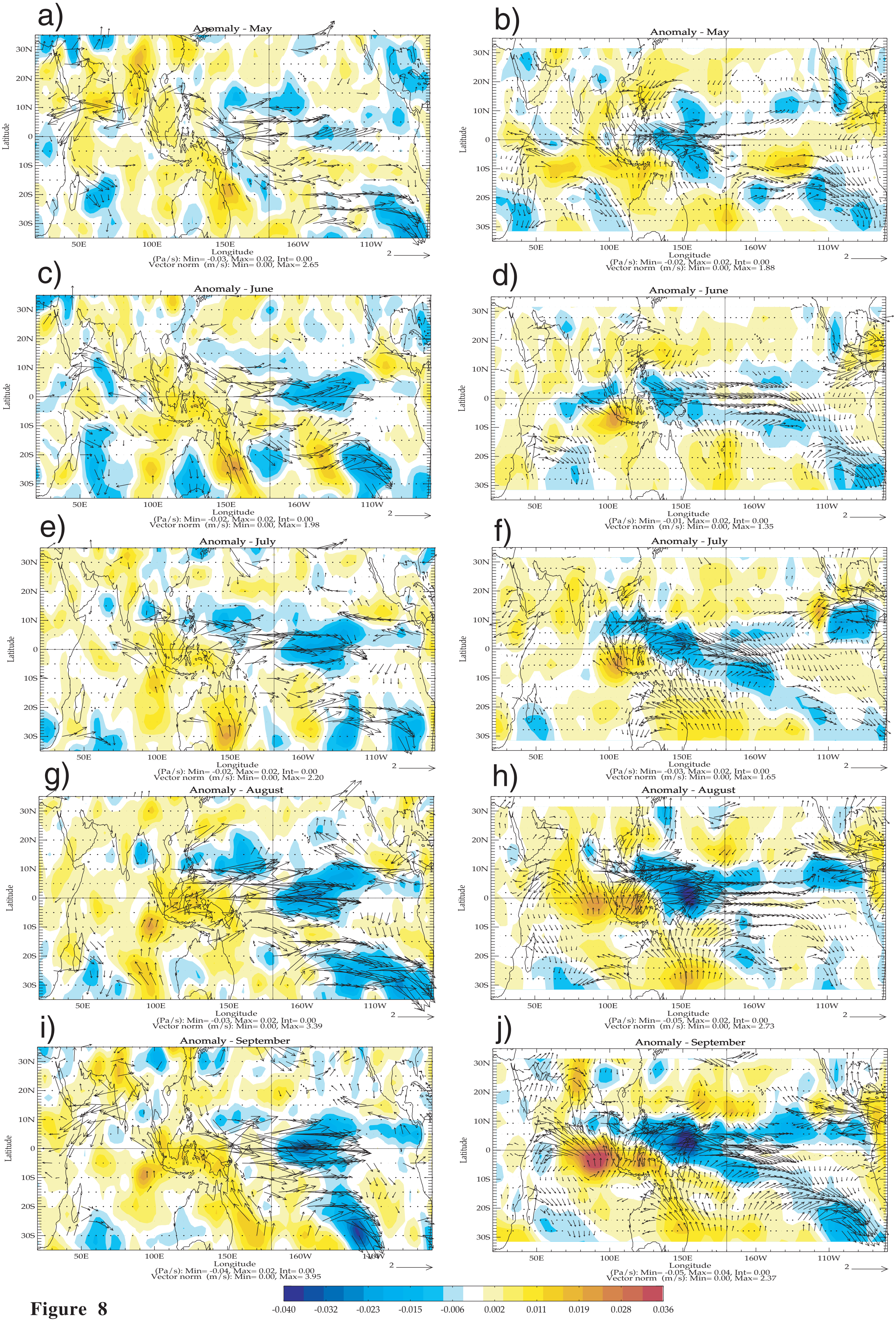
a)
Anomaly - May
(Pa/s): Min= -0.03, Max= 0.02, Int= 0.00
Vector norm (m/s): Min= 0.00, Max= 2.65
b)
Anomaly - May
(Pa/s): Min= -0.02, Max= 0.02, Int= 0.00
Vector norm (m/s): Min= 0.00, Max= 1.88
c)
Anomaly - June
(Pa/s): Min= -0.02, Max= 0.02, Int= 0.00
Vector norm (m/s): Min= 0.00, Max= 1.98
d)
Anomaly - June
(Pa/s): Min= -0.01, Max= 0.02, Int= 0.00
Vector norm (m/s): Min= 0.00, Max= 1.35
e)
Anomaly - July
(Pa/s): Min= -0.02, Max= 0.02, Int= 0.00
Vector norm (m/s): Min= 0.00, Max= 2.20
f)
Anomaly - July
(Pa/s): Min= -0.03, Max= 0.02, Int= 0.00
Vector norm (m/s): Min= 0.00, Max= 1.65
g)
Anomaly - August
(Pa/s): Min= -0.03, Max= 0.02, Int= 0.00
Vector norm (m/s): Min= 0.00, Max= 3.39
h)
Anomaly - August
(Pa/s): Min= -0.05, Max= 0.02, Int= 0.00
Vector norm (m/s): Min= 0.00, Max= 2.73
i)
Anomaly - September
(Pa/s): Min= -0.04, Max= 0.02, Int= 0.00
Vector norm (m/s): Min= 0.00, Max= 3.95
j)
Anomaly - September
(Pa/s): Min= -0.05, Max= 0.04, Int= 0.00
Vector norm (m/s): Min= 0.00, Max= 2.37
Latitude
30N
20N
10N
0
10S
20S
30S
Longitude
50E
100E
150E
160W
110W
2
-0.040
-0.032
-0.023
-0.015
-0.006
0.002
0.011
0.019
0.028
0.036

Figure 8

Figure 9

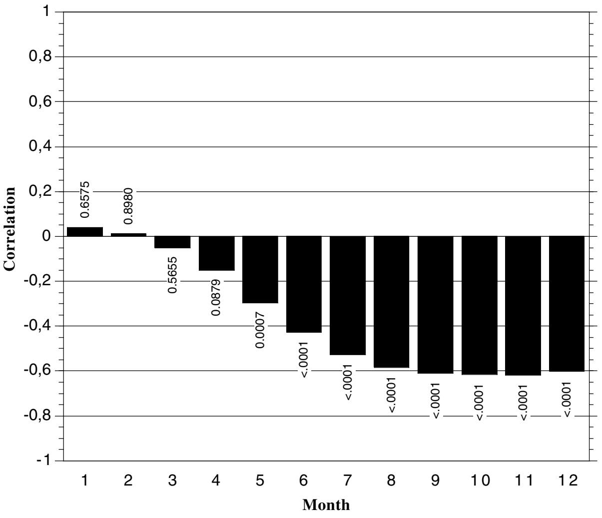

a) Lead/lag correlations between
monthly Nino34 SST and ISM rainfall time series
(Data, 128 years)

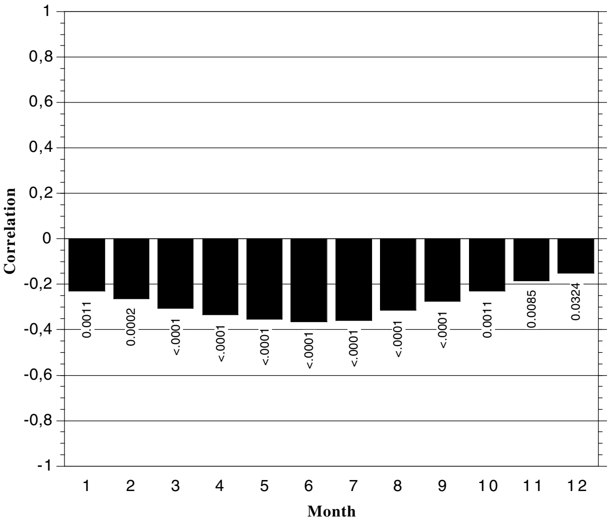

b) Lead/lag correlations between
Monthly Nino34 SST and ISM rainfall time series
(SINTEX coupled model, all years)

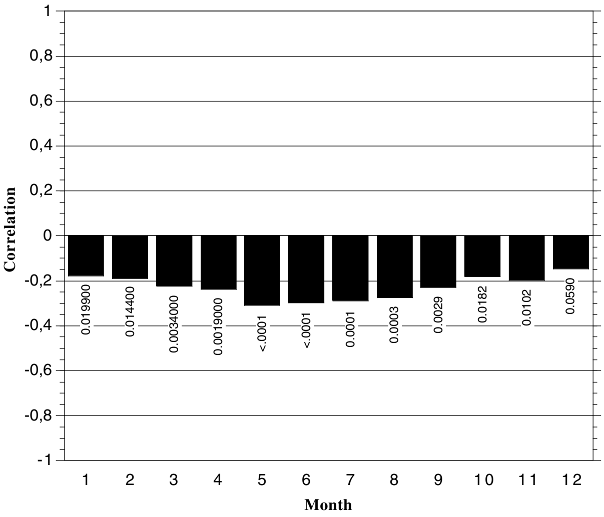

c) Lead/lag correlations between
Monthly Nino34 SST and ISM rainfall time series
(SINTEX coupled model, no aborted ENSO years)

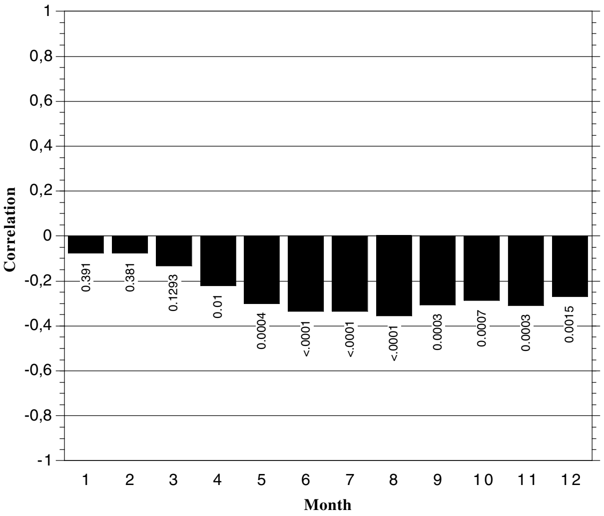

d) Lead/lag correlations between
Monthly Nino34 SST and ISM rainfall time series
(SINTEX coupled model, no aborted ENSO years, no El Nino years +1)

Figure 10

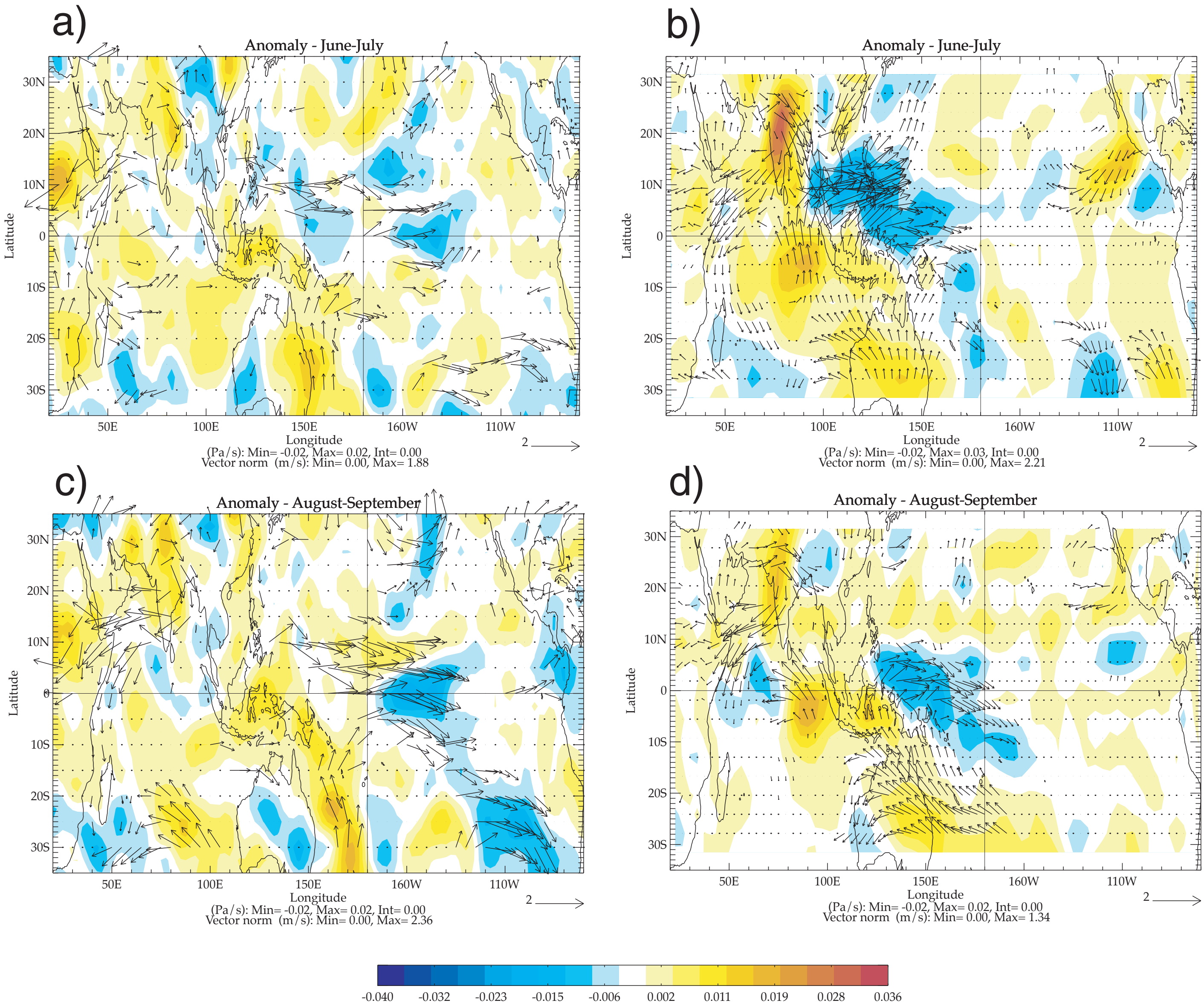
a)
Anomaly - June-July
30N
20N
10N
0
10S
20S
30S
Latitude
50E
100E
150E
160W
110W
Longitude
2
(Pa/s): Min= -0.02, Max= 0.02, Int= 0.00
Vector norm (m/s): Min= 0.00, Max= 1.88
b)
Anomaly - June-July
Latitude
Longitude
(Pa/s): Min= -0.02, Max= 0.03, Int= 0.00
Vector norm (m/s): Min= 0.00, Max= 2.21
c)
Anomaly - August-September
Latitude
Longitude
(Pa/s): Min= -0.02, Max= 0.02, Int= 0.00
Vector norm (m/s): Min= 0.00, Max= 2.36
d)
Anomaly - August-September
Latitude
Longitude
(Pa/s): Min= -0.02, Max= 0.02, Int= 0.00
Vector norm (m/s): Min= 0.00, Max= 1.34
-0.040
-0.032
-0.023
-0.015
-0.006
0.002
0.011
0.019
0.028
0.036

Figure 11

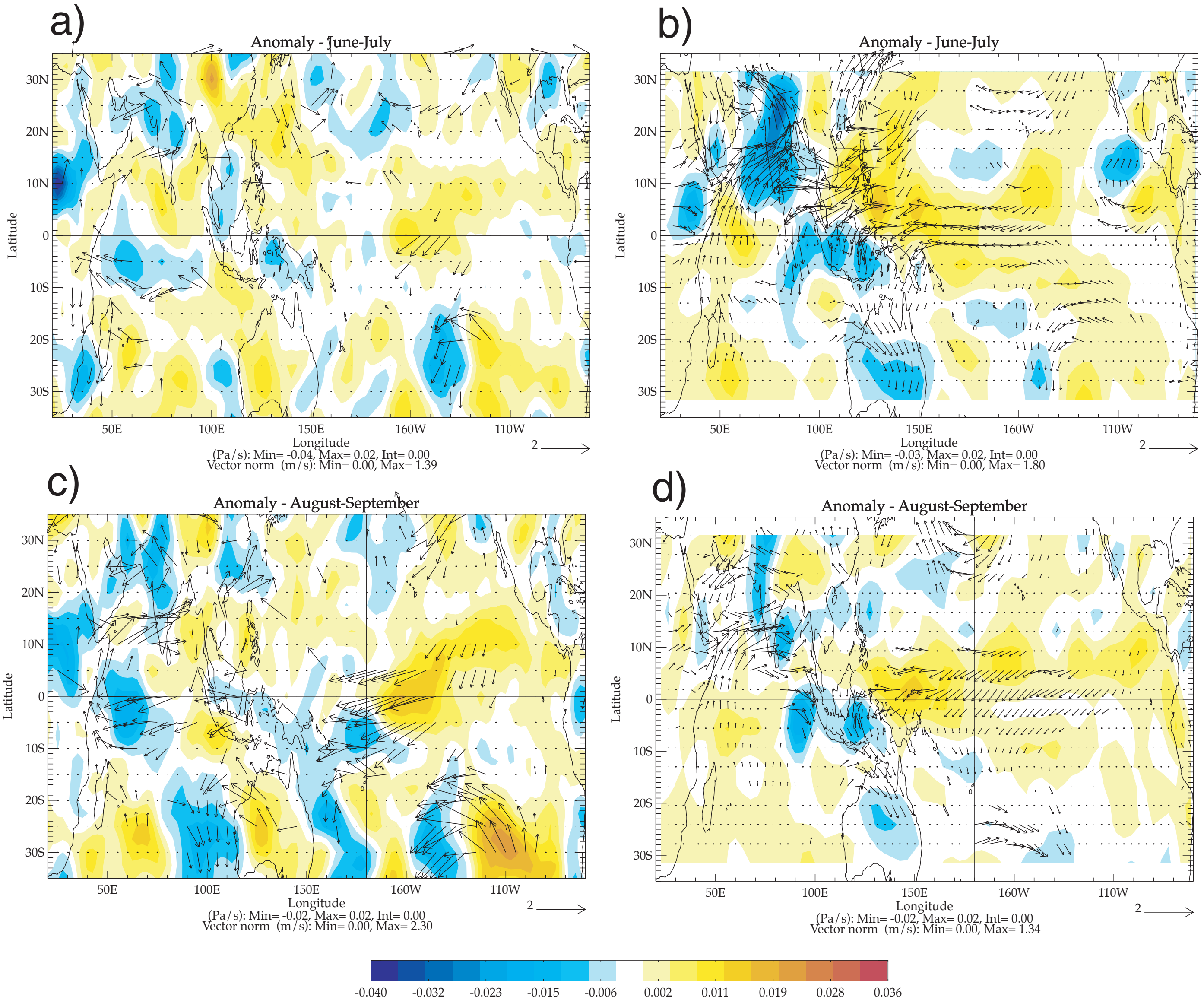
a)
Anomaly - June-July
Latitude
30N
20N
10N
0
10S
20S
30S
50E
100E
150E
160W
110W
Longitude
2
(Pa/s): Min= -0.04, Max= 0.02, Int= 0.00
Vector norm (m/s): Min= 0.00, Max= 1.39
b)
Anomaly - June-July
Latitude
Longitude
2
(Pa/s): Min= -0.03, Max= 0.02, Int= 0.00
Vector norm (m/s): Min= 0.00, Max= 1.80
c)
Anomaly - August-September
Latitude
Longitude
2
(Pa/s): Min= -0.02, Max= 0.02, Int= 0.00
Vector norm (m/s): Min= 0.00, Max= 2.30
d)
Anomaly - August-September
Latitude
Longitude
2
(Pa/s): Min= -0.02, Max= 0.02, Int= 0.00
Vector norm (m/s): Min= 0.00, Max= 1.34
-0.040
-0.032
-0.023
-0.015
-0.006
0.002
0.011
0.019
0.028
0.036

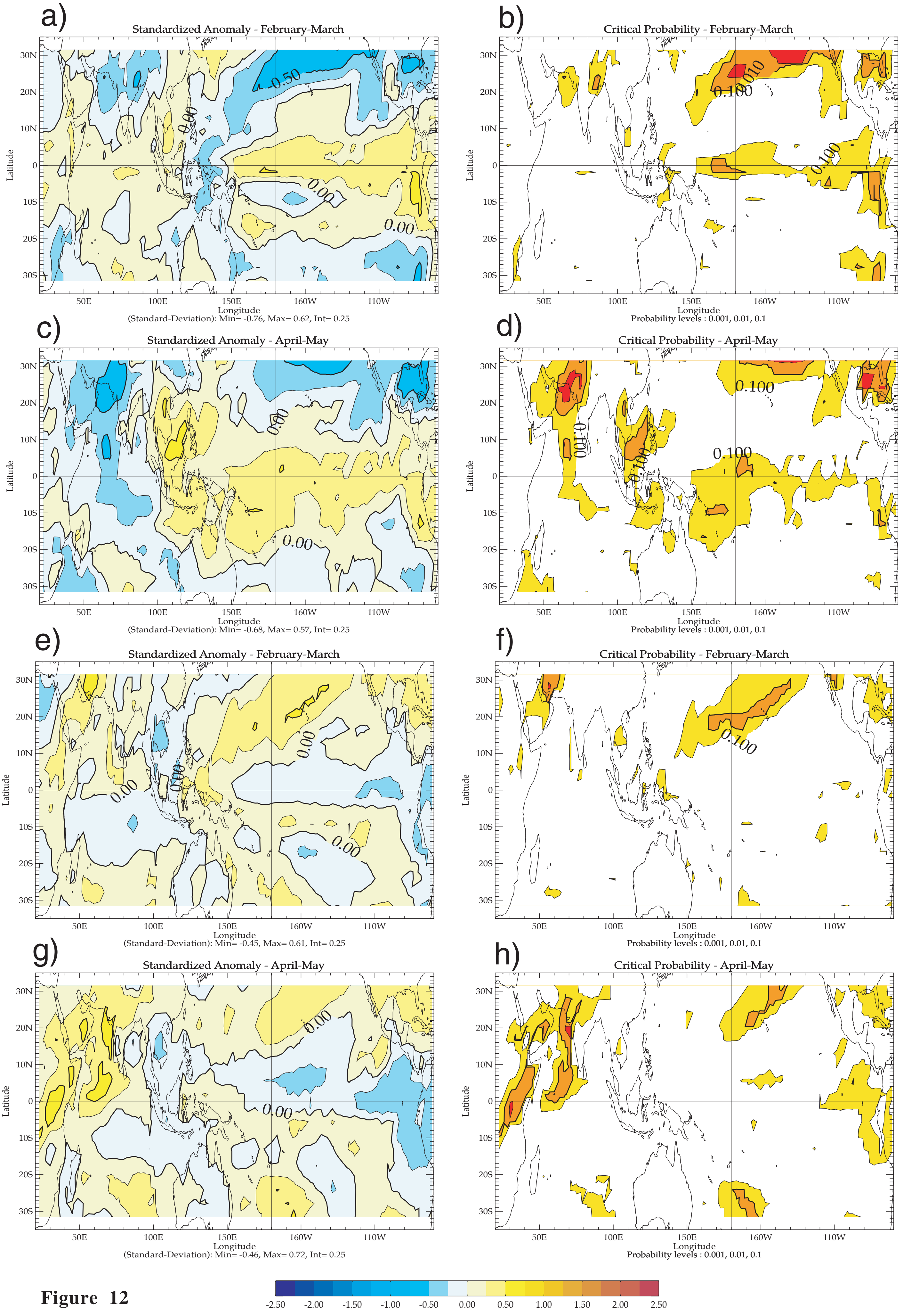
a)
Standardized Anomaly - February-March
b)
Critical Probability - February-March
c)
Standardized Anomaly - April-May
d)
Critical Probability - April-May
e)
Standardized Anomaly - February-March
f)
Critical Probability - February-March
g)
Standardized Anomaly - April-May
h)
Critical Probability - April-May
Latitude
Longitude
30N
20N
10N
0
10S
20S
30S
50E
100E
150E
160W
110W
-0.50
0.00
0.100
0.010
(Standard-Deviation): Min= -0.76, Max= 0.62, Int= 0.25
(Standard-Deviation): Min= -0.68, Max= 0.57, Int= 0.25
(Standard-Deviation): Min= -0.45, Max= 0.61, Int= 0.25
(Standard-Deviation): Min= -0.46, Max= 0.72, Int= 0.25
Probability levels : 0.001, 0.01, 0.1
-2.50
-2.00
-1.50
-1.00
-0.50
0.00
0.50
1.00
1.50
2.00
2.50

Figure 12

Figure 13

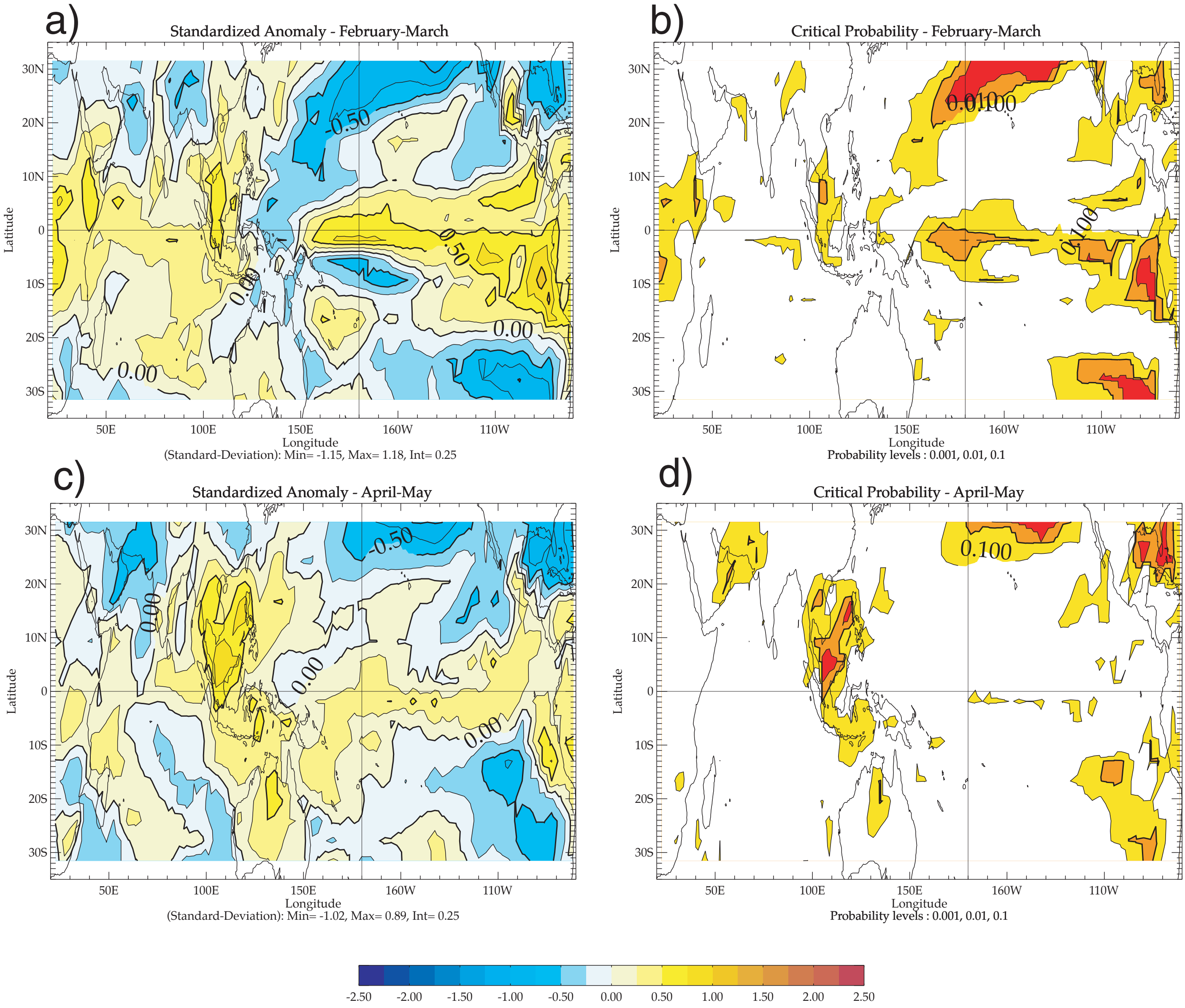

Weak ISM Temperature composite - No ENSO - SINTEX - Year 0,

a) Standardized Anomaly - February-March

(Standard-Deviation): Min= -1.15, Max= 1.18, Int= 0.25

b) Critical Probability - February-March

Probability levels : 0.001, 0.01, 0.1

c) Standardized Anomaly - April-May

(Standard-Deviation): Min= -1.02, Max= 0.89, Int= 0.25

d) Critical Probability - April-May

Probability levels : 0.001, 0.01, 0.1

Figure 14

a)

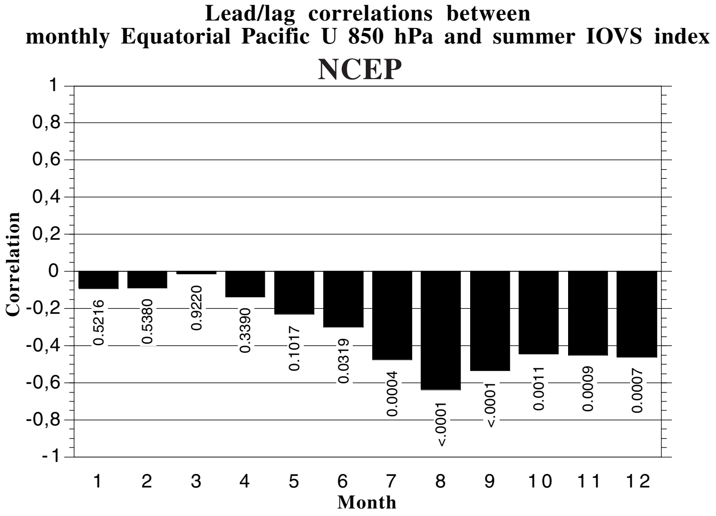

Lead/lag correlations between
monthly Equatorial Pacific U 850 hPa and summer IOVS index

NCEP

b)

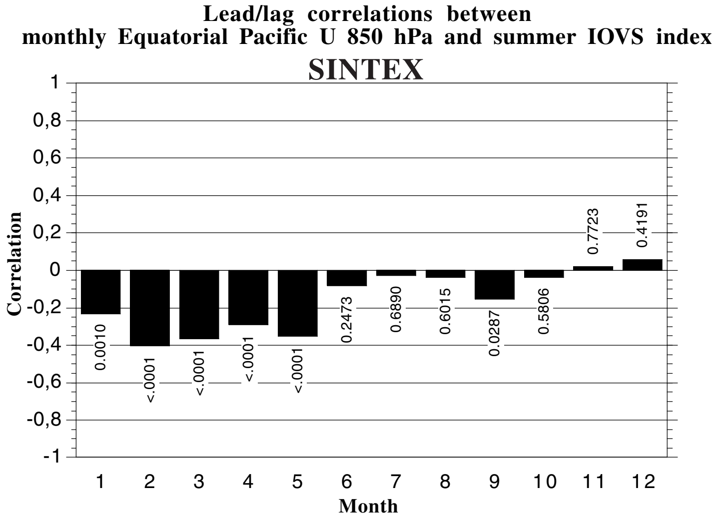

Lead/lag correlations between
monthly Equatorial Pacific U 850 hPa and summer IOVS index

SINTEX